Research configuration to study shock oscillation mechanisms in highly loaded transonic fans

Nel, Philipp L.; Schreyer, Anne Marie; Schrijer, Ferry F.J.; van Oudheusden, Bas W.; Swoboda, Marius

DOI
10.1016/j.ast.2025.110636

Publication date
2025

Document Version
Final published version

Published in
Aerospace Science and Technology

Citation (APA)
Nel, P. L., Schreyer, A. M., Schrijer, F. F. J., van Oudheusden, B. W., & Swoboda, M. (2025). Research configuration to study shock oscillation mechanisms in highly loaded transonic fans. *Aerospace Science and Technology*, *166*, Article 110636. https://doi.org/10.1016/j.ast.2025.110636

Aerospace Science and Technology 166 (2025) 110636

Contents lists available at ScienceDirect

Aerospace Science and Technology

journal homepage: www.elsevier.com/locate/aescte

Original article

Research configuration to study shock oscillation mechanisms in highly loaded transonic fans

Philipp L. Nel [a,*], Anne-Marie Schreyer [b], Ferry F.J. Schrijer [c], Bas W. van Oudheusden [c], Marius Swoboda [d]

[a] RWTH Aachen University, Institute of Jet Propulsion and Turbomachinery, Templergraben 55, Aachen, 52062, North Rhine-Westphalia, Germany
[b] Munich University of Applied Sciences, Faculty 3, Dachauer Straße 98b, Munich, 80335, Bavaria, Germany
[c] Delft University of Technology, Faculty of Aerospace Engineering, High Speed Aerodynamics Laboratory, Kluyverweg 1, Delft, 2629 HS, South Holland, Netherlands
[d] Rolls-Royce Germany Ltd. & Co. KG, Blankenfelde-Mahlow, Brandenburg, 15827, Brandenburg, Germany

ARTICLE INFO

Communicated by Kivanc Ekici

Keywords:
Shock oscillation
Large eddy simulation
Transonic fans
Oscillation mechanism

ABSTRACT

The design of transonic compressors increasingly focuses on higher blade loading, sparking interest in shock oscillation mechanisms in highly loaded transonic fans operating at cruise altitude. At such conditions, low chord Reynolds numbers (1.4 Mio.) may sustain a laminar boundary layer on the suction side of the blade up to the shock-wave/boundary-layer interaction (SBLI). The resulting interaction with large separation (pre-shock Mach number of 1.6) cause shock oscillations and structural excitation. In this study, we demonstrate that a canonical research configuration enables the experimental investigation of a specific shock oscillation mechanism relevant to transonic fans at altitude, providing a basis for validation. Using Large Eddy Simulations and experimental data, we show that the oscillation mechanism depends on the conditions at the SBLI rather than the geometry. The oscillation arises from the growth and self-suppression of the upstream laminar section of the separation bubble. Periodic collapse of this laminar section generates turbulence that entrains the separation bubble, influencing the dynamics of the reflected shock. The reflected shock movement resembles the cascade passage shock behavior, driven by blockage variations from the separation bubble. Additionally, we examine the numerical requirements to resolve this mechanism. These findings provide insights to advance compressor designs and hypersonic applications featuring similar mechanisms.

1. Introduction

Typically, modern business jets operate at higher altitudes (15-16 km) than commercial aircraft (10-13 km), taking advantage of avoiding air traffic associated with commercial flights, less turbulence, and lower drag (lower air density). At 15 km, the air density drops by 50% from its value at 10 km. Additionally the transonic fan blade chord length on a business jet is about half that of commercial aircraft, hence the chord Reynolds number is lower. On top of that, the atmosphere is quieter at altitude (lower turbulence). All of these factors contribute to a laminar boundary layer persisting on the suction side of the transonic fan and interacting with the shock wave at altitude, rather than a turbulent one as is otherwise the case [1].

Additionally, with an ever increasing need for higher loading and lighter engines to obtain higher efficiency [1–3], shock-wave/boundary-layer interactions play an increasingly significant role in business jet engines, as well as in military applications operating at similar altitudes (such as fighter jets and long range bombers). Higher blade loading results in stronger shock-wave/boundary-layer interactions, causing increased separation and shock unsteadiness. Furthermore, reduced weight may mean easier excitation of the blade structure. The shock unsteadiness frequency may be similar to the blade's structural natural frequencies, causing vibrations if this shock oscillation mechanism is not suppressed. Shock oscillations in transonic fans and cascades are not well understood [4]. For reference to common nomenclature, common shock structures in transonic compressors are shown in Fig. 1 [5].

In Nel et al. [6] the effect of transition and different shock structures on the shock oscillation in a transonic cascade was investigated. It was concluded that the experimental cascade setups did not show the shock oscillation mechanism of interest, since there is no significant difference in shock travel distance between a laminar and turbulent SBLI

* Corresponding author.
E-mail address: nelphilipp@gmail.com (P.L. Nel).

https://doi.org/10.1016/j.ast.2025.110636
Received 26 February 2025; Received in revised form 28 June 2025; Accepted 12 July 2025
Available online 17 July 2025

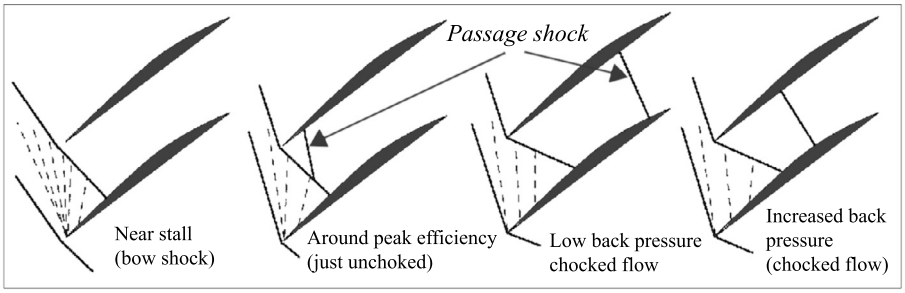

Fig. 1. Shock structures across the working range of transonic compressors (adapted from Denton and Xu [5]).

in the case of the experiments, whereas it was expected from engine altitude tests that a turbulent SBLI shows a mitigated shock oscillation. This claim that the cascade in a wind tunnel facility is supported by the fact that the bow shock condition, with a very small separation, oscillates to a large extent and at roughly the same frequency as the highly loaded condition, whereas the bow shock condition with a small separation does not oscillate in Large Eddy Simulations (LES) or Direct Numerical Simulations (DNS) with a clean inflow [6–11], indicative additional oscillation mechanisms in the experiment. None of the mentioned studies include an experimental validation of the shock oscillation mechanism observed in the numerical simulations - the purpose of the current work. It is difficult to recreate the mechanism occurring at quiet flight altitude conditions (similar to simulations with laminar inflow) in a practical wind tunnel experiment due to the inherent high turbulence levels of wind tunnels, which inherently exhibit significant upstream flow disturbances. We therefore aspire to derive a simplified generic configuration that exhibits the same oscillation mechanism as the LES with quiet inflow on a cascade. With this configuration, the oscillation mechanism can be studied experimentally and the dynamic behavior observed in the LES calculations (periodic growth and eventual collapse of the shock induced separation upstream laminar section, causing shock oscillation) can be validated. The objective of this work is to define this case and demonstrate the equivalence between the shock oscillation mechanism of this canonical configuration and that of the highly loaded transonic cascade.

The simplification of the problem of shock oscillation to a canonical form that can be studied experimentally, starts with a multi-passage transonic cascade (configuration *a* in Fig. 2), and leads to a highly separated oblique SBLI with transition on the upstream shear layer (configuration *f* in Fig. 2). The intermediate steps which were followed to simplify the configuration step by step while ensuring equivalence of the oscillation mechanism and arrive at the final configuration are also summarized in Sec. 3.1. More detail on the transonic channel configuration *c* and *d* can be found in literature [12,6,13]. All of the cases in Fig. 2 show the same shock oscillation mechanism, which is suppressed when tripping the boundary layer. In the current work, we will focus on cases *a*, *b*, *e*, and *f*, with an emphasis on showing the equivalence of the highly loaded transonic cascade setup (*b*) to the canonical configuration (*f*). In all of the cases, the laminar separation shock (indicating a laminar section of the separation bubble) periodically forms with comparable upstream propagation velocities. This thin, long section of the laminar separation bubble collapses at a point when the turbulence which is generated on its shear layer suppresses this section of the separation bubble, causing a temporary collapse and reset of the oscillation. As we will show in Sec. 4.4, a turbulent boundary layer leads to the elimination of this mechanism. This holds for all of the cases, considering that the elimination of the mechanism for a turbulent oncoming boundary layer was already shown in Nel et al. [6].

A considerable advantage of the canonical configuration is the small domain needed relative to a transonic cascade, which considers the leading and trailing edge as well as the blade pressure side, which are not important for the existence of the shock oscillation mechanism. In the current work, we go into more detail with regard to numerical requirements, since a comparison to a DNS-resolution case is also considered. The current work serves as the link between the work performed on cascades [6] and that performed on the canonical research configuration [14,15].

The article is structured as follows: in Sect. 2 we discuss how the boundary conditions that show the oscillation mechanism of interest were arrived at. In Sect. 3, we explain the derivation of the canonical research configuration. Since establishing an initial standard for numerical requirements is important before performing LES on the final experimental conditions, we investigate numerical requirements for resolving the shock oscillation mechanism in Sect. 4 by comparing solutions of different grid resolution and subgrid-scale models to a DNS-resolution solution. In Sect. 4 we investigate the shock oscillation mechanism features in detail and compare the laminar oncoming boundary layer case to a turbulent case. This aims to confirm that elimination of the shock oscillation mechanism for the canonical research configuration is consistent with the transonic cascade case. Experimental shadowgraph and Schlieren results from the canonical research configuration are presented in Sect. 5 for a qualitative comparison of the experimental SBLI behavior to the LES results. Finally, we discuss the conclusions and outlook in Sect. 6.

In concurrent work by the authors [14,15], the experiment studying the canonical configuration (*f*) is realized at Delft University of Technology. High speed Schlieren and spark light shadowgraphy were used to investigate the mechanisms and dynamics of the shock oscillation and the shifting transition location on the separated shear layer. Nel et al. [15] showed matching Strouhal numbers of the shock oscillation in the canonical case, basing the characteristic length on the travel distance of the laminar separation shock [15]. This study was supported by particle image velocimetry [14], confirming the separation shock behavior at mid-span and quantifying the separation bubble and Mach stem size variation.

2. Numerical methods and boundary conditions for LES cascade simulations

The numerical simulations are performed with the Rolls-Royce *HYDRA* code [16], which uses second order accurate spatial and implicit dual time stepping schemes. For consistency, we consider inviscid endwalls in all LES cases, due to the transonic cascade case requiring an inviscid endwall contraction to account for the correct axial velocity density ratio (AVDR), which prohibits spanwise periodic boundary conditions. Pitch-wise periodic boundary conditions are implemented for cascade LES and full-span fan RANS simulations.

The definition of LES boundary conditions begins with a steady RANS simulation of the full-span fan. The full-span fan setup (Fig. 4) is simulated at the operating condition corresponding to the largest excitation observed in altitude strain gauge vibration measurements. The resulting flow field reveals a pre-shock Mach number of approximately 1.6 and a passage-shock structure characterized by significant separation (Fig. 5).

To replicate these flow features in a practical computational domain for LES, a quasi-2D domain with inviscid end walls is defined. Although 3-dimensional behavior of the shock movement in a full span transonic

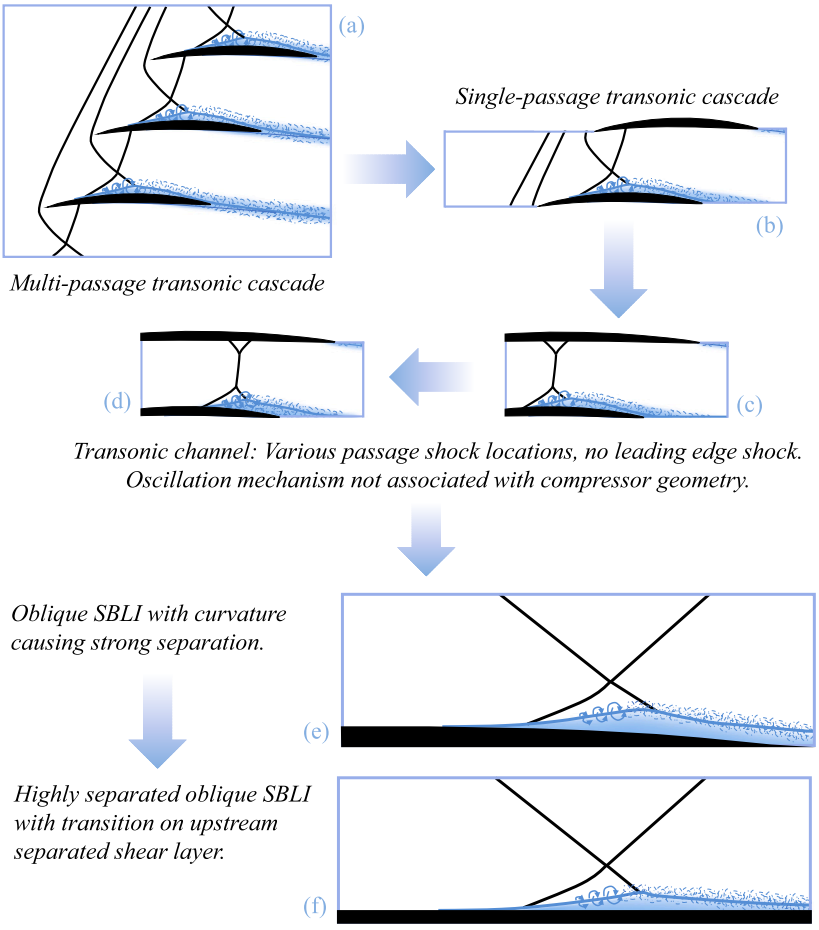

Fig. 2. Simplification of low Reynolds transonic fan shock oscillation problem to a canonical configuration.

fan is likely present due to the Mach number and separation varying along the span, the source of the shock oscillation mechanism studied in the present work does is not dependent on spanwise effects. Nel et al. [17] demonstrated that the frequency and behavior remain unaffected by the spanwise extent of the quasi-2D domain, based on a comparison between cases with 20% and 30% chord in the spanwise direction. Quasi-2D compressor cascades are widely used as simplifications to full span applications [7,18,8–11,19]. The domain in the present study incorporates end-wall contraction, as described by Nel et al. [13], ensuring consistency with prior calculations [6,20] and existing experimental setups for the cascade geometry at the German Aerospace Centre and the Institute of Fluid Flow Machinery, Polish Academy of Sciences (IMP PAN) [20] (see Fig. 3). The domain has a width of 20% of the chord in the spanwise direction.

In the LES calculations, Δx^+ and Δz^+ values are around 25 for a case at Re = 350 000, and 50 for a case at Re = 1.4 million, with Δy^+ ranging between 1 and the aforementioned values. In terms of isentropic Mach number distribution on a cascade, RANS and LES validation has been performed in Nel et al. [6] for the current numerical setup and demonstrates insensitivity to the grid.

When simulating the condition arrived at through the RANS simulation of the full span fan in the LES cascade setup, the flow field demonstrates a pronounced shock oscillation [6,17], which is further examined in the present study. Nel et al. [6] also showed that the oscillation in the transonic cascade LES is mitigated by tripping of the boundary layer, a technique which is already used in the industrial application, although up to now it has not been clear why this solves the issue.

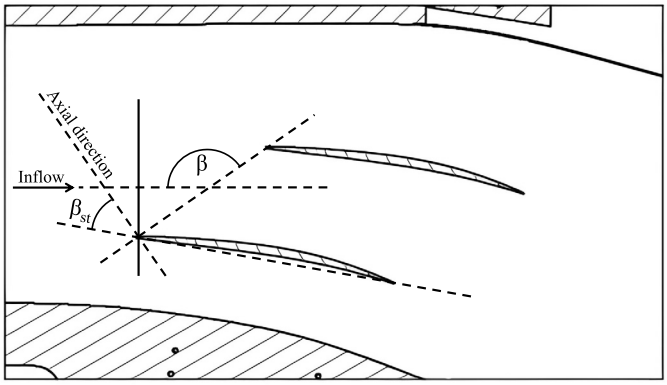

Fig. 3. Sketch of TFAST cascade setup at IMP PAN (β_{st} is the stagger angle of 44.39°, and β is the flow angle with respect to cascade front, used for the AVDR).

3. Derivation of simplified canonical configuration

Now that we have defined the flow conditions, we focus on the shock oscillation and begin the process of simplifying the geometry as much as possible. We first establish that the mechanism of shock oscillation is analogous between a periodic triple-passage cascade setup (Fig. 2 (a)) and the single-passage setup (Fig. 2 (b)), which allows a simplification to a single passage by confirming that the oscillation mechanism source is not associated with multi-passage effects. In order to show the shock oscillation in more detail in the time domain, we plot the Mach number over time for multiple offsets from the suction side of the profile. The

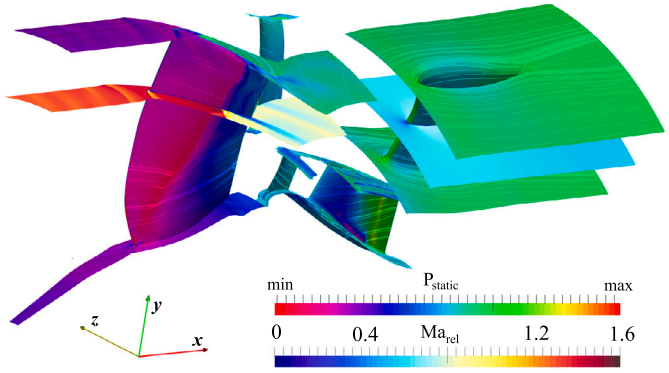

Fig. 4. Full span fan domain.

interrogation lines used for plotting the cascade results are illustrated in Fig. 6.

In the triple passage case, these lines are applied to each passage of the cascade and the Mach number is plotted over time for two oscillation cycles after 10 convective time steps (Fig. 7). Each row of the plot contains a different passage, and each column contains a cut according to Fig. 6 in the middle of each passage. The cut at 3.3% chord above the suction side surface corresponds approximately to the mean separation height.

The results for the triple passage cascade case are shown in Fig. 7. In these plots, the laminar separation shock region can be seen as a distinct supersonic region which is shifting, and extending to just over 0.2 x/c beyond the separated or turbulent regions. In the first offset (Offset 1 in Fig. 7), the cut is parallel to the blade suction side at a distance of 1.8% of the chord length, and passes through a lower portion of the separation bubble, intersecting with the upstream laminar segment of the shear layer. This laminar section of the separation bubble grows upstream, carrying instabilities along the shear layer. Eventually, this becomes too elongated such that it gets suppressed by its own instabilities.

The shock oscillation mechanism still persists, even if the laminar section of the separation bubble is not completely suppressed by the turbulence on the shear layer, noted by the fact that in this cut, we consistently see a laminar cut through the shear layer. The partial or complete suppression of the upstream laminar section of the separation becomes more apparent in the isentropic Mach number distribution plots, which are analyzed after the standard Mach number comparison.

In the second offset, the plot shows a cut through a turbulent part of the shear layer. In the third offset, the effect of separation bubble suppression becomes evident. During the forward shift of the shock wave and transition, a turbulent, separated region with low Mach numbers cuts through the separation bubble. In contrast, during the backward movement, a supersonic expansion region forms over the separation bubble, just downstream of the shock wave, which is distinctively visible only during this stage. In the fourth offset, the shock wave remains present throughout the oscillation cycle. A pronounced expansion region appears in the downstream stage, due to a flatter separation bubble in this area. Notably, the oscillation phases are synchronized between the passages.

Next, the triple-passage case (Fig. 7) is compared to the single-passage case (Fig. 8). Similar flow features are observed, consistent with the preceding discussion, though the amplitude of oscillation is larger in the single-passage case (0.15 chord vs. 0.1 chord). This is likely due to the absence of natural damping from neighboring passages, as competing shock oscillation phases are not present. The fact that the shock oscillation persists for both cases allows the simplification to a single passage cascade for a more in depth study, since the single passage computation is less expensive.

To present the oscillation flow characteristics over time in more detail, we examine the isentropic Mach number in Fig. 9. Note the pronounced laminar separation shock signature for the upstream propagating state (green area in Fig. 9), indicating a larger deflection angle through the laminar separated shear layer. The weaker, vanishing laminar separation shock for the downstream-movement state indicates a “flat”, near-tangential retreat of the separation bubble as opposed to flow deflection at a steep angle from the blade surface. This suggests a pronounced laminar section for the upstream propagating state, and a vanishing laminar section for the retreating state of the oscillation as a result of suppression of this elongated upstream section through shear layer instabilities once a certain, critical length is reached where the instabilities on the thin, elongated section are significant enough to cut off this section (fully or in part, likely dependent on the Reynolds number). Once the retreat of the shock and separation is completed to a downstream position, briefly displaying an almost turbulent-SBLI state,

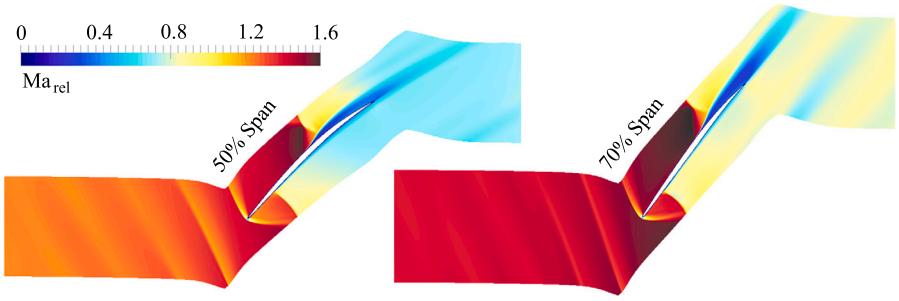

Fig. 5. Flow in a transonic compressor: full span RANS simulation, cuts at 50% and 70% span showing contours of Mach number. Reproduced from Nel et al. [6].

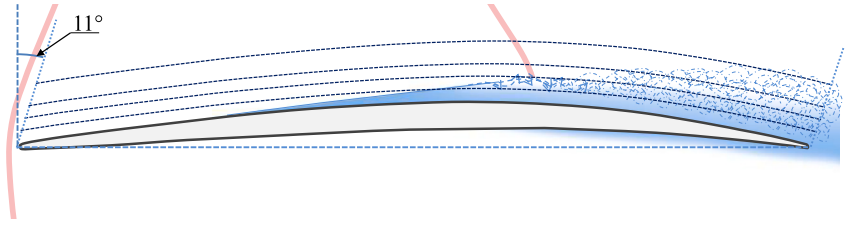

Fig. 6. Relation of the interrogation lines to the chord, with the suction-side-profile-shaped lines positioned 1.8, 3.3, 4.8 and 7.8% chord above the suction side surface.

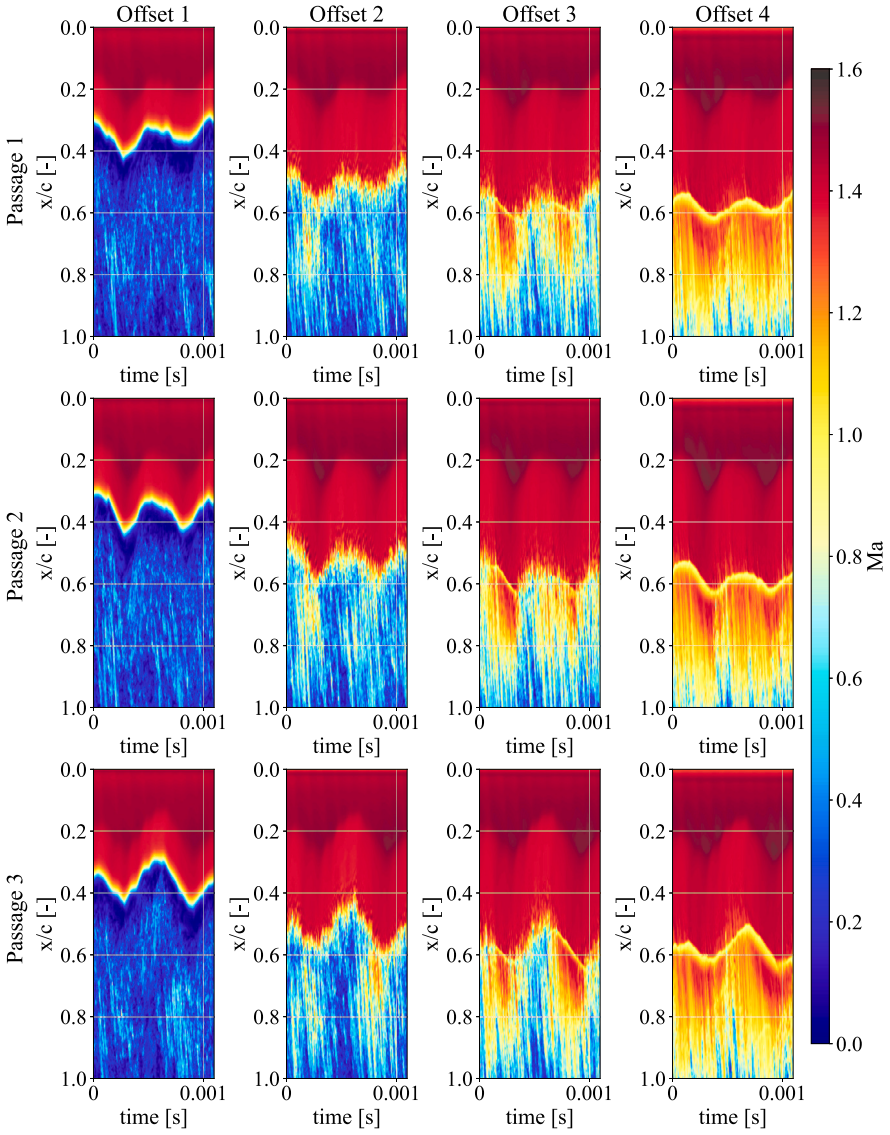

Fig. 7. Triple passage cascade: Mach number distributions in time for each passage along specific offsets above the profile suction side. From left to right: 1.8%, 3.3%, 4.8% and 7.8% chord above the suction side.

the shock oscillation cycle can repeat, since the instabilities have advected downstream, meaning the growth of a laminar shear layer is no longer suppressed. Furthermore, we note the shifting transition location, evident through the high frequency-free laminar region leading to a turbulent region which shifts during the oscillation cycle.

Until now, we considered a reduced Reynolds number, as it was previously seen that both reduced (350 000) and original Reynolds number (1 400 000) cases produce the same shock oscillation in terms of Strouhal number, with the length scale based on blade chord length [6]. The isentropic Mach number plotted with time for the original Reynolds number case can be seen in Fig. 10, where one can observe an analogous behavior as that discussed for the reduced Reynolds number case (Fig. 9). Dynamic mode decomposition on the mid-section pressure field extracts shock oscillation modes at a Strouhal number around 0.1 for both cases [13].

The transonic channel case [12,6,13] (Fig. 2(c) and (d)), shows the same oscillation mechanism as in the cascade, despite the simplification of having no leading edge and leading edge shock wave (Fig. 11). The separation shock periodically forms and moves upstream at a comparable order of velocity to the compressor cascade case. The oscillation amplitude is once again greatly reduced when tripping the boundary layer [13]. The findings suggest that the shock oscillation mechanism is not inherent to the compressor-like suction side blade curvature. This allows for a further simplification of the problem in order to arrive at the canonical research configuration.

3.1. Canonical configuration

We showed that regardless of the geometry, the same oscillation mechanism exists, having to do with laminar separation bubble growth and collapse, due to upstream propagating shear layer instabilities on the separation causing turbulent suppression nearing the end of the separation bubble growth phase. The shock oscillation mechanism is therefore rather a function of the conditions at the interaction itself than of the geometry. Furthermore, in Nel et al. [6], it was concluded that a more canonical experimental case is needed in order to validate and study the mechanism experimentally, since the cascade experiments appeared to exhibit too many additional sources of shock oscillation, and hence cannot be compared with the CFD with laminar inflow to simulate the quiet altitude conditions. Therefore, we further simplify the case, to arrive at the most canonical case where this type of shock oscillation can be seen. The reader is once again referred to the problem simplification diagram at the beginning of the chapter (Fig. 2). Since the case simplifi-

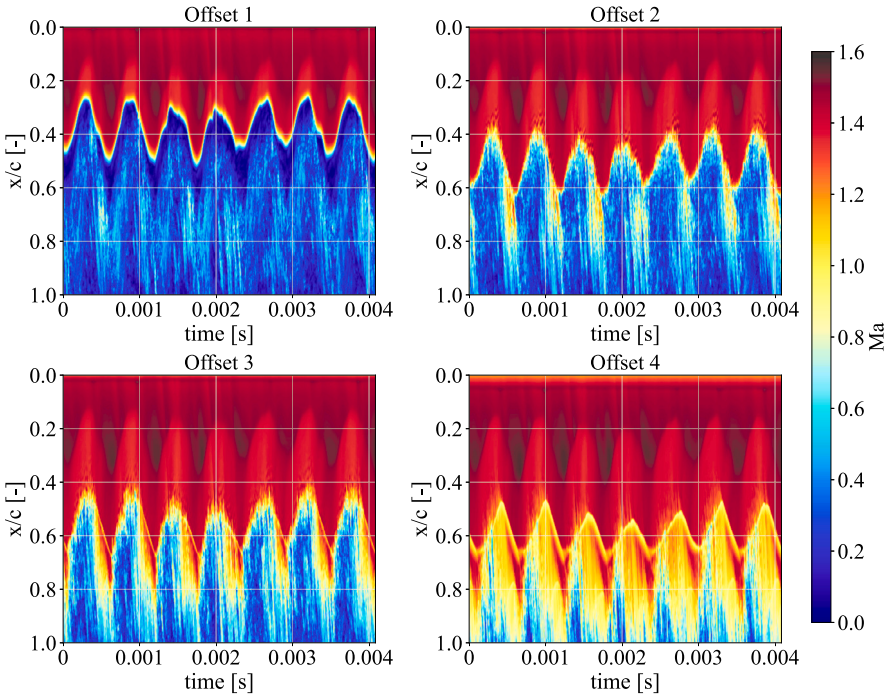

Fig. 8. Single passage cascade: Mach number distributions in time along specific offsets above the profile suction side. First to last offset: 1.8%, 3.3%, 4.8% and 7.8% chord above the suction side.

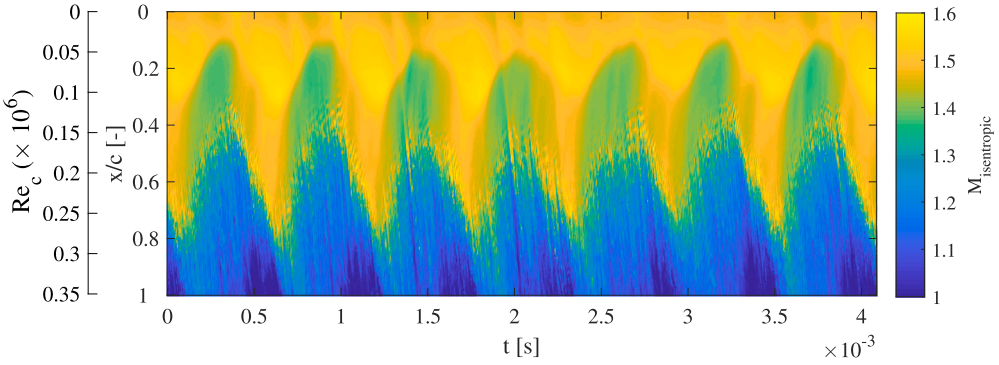

Fig. 9. Single passage cascade (reduced Reynolds number): suction side isentropic Mach number distribution in time. (For interpretation of the colors in the figure(s), the reader is referred to the web version of this article.)

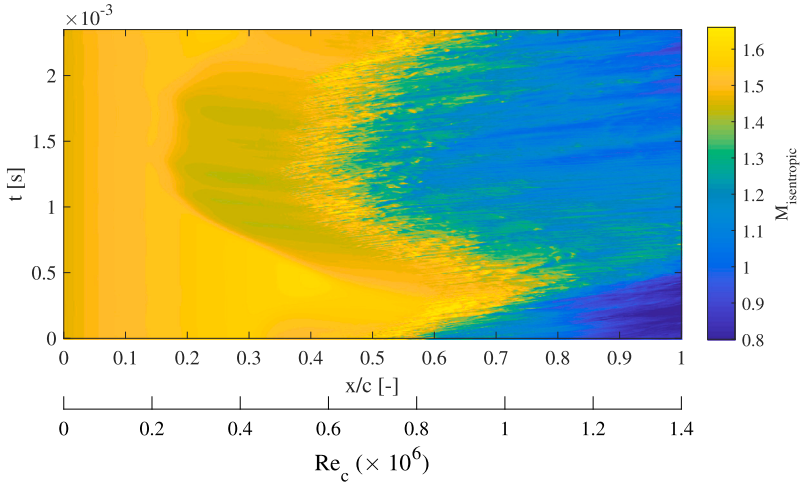

Fig. 10. Single passage cascade (reduced Reynolds number): suction side isentropic Mach number distribution in time (one oscillation cycle).

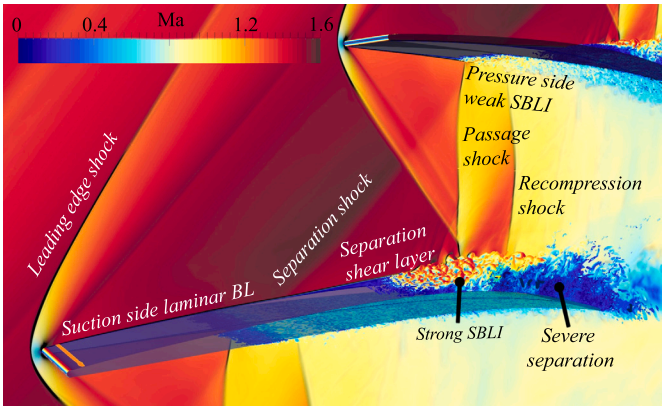

Fig. 11. Nomenclature for shock structure in transonic compressor. Re 1.4 Mio. LES simulation with laminar SBLI.

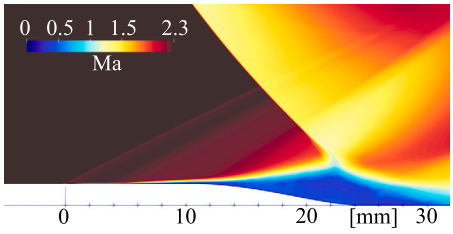

Fig. 12. Oblique SBLI impinging on curvature: Ma = 2.3, $\theta = 24^{\circ}$, time averaged Mach number contours.

cation comes from the transonic compressor background, the next step in the simplification is to remove the suction side compressor-like curvature and study whether there is a fundamental effect on the oscillation source.

In the cascade LES investigations of Sect. 3, it was also seen that the oscillation source is independent of the leading edge shock wave, since the leading edge shock wave is steady unless the separation shock foot reaches the leading edge (for details see Nel [13]). Furthermore, the oscillation mechanism is not present for a small separation, for example the bow shock condition. In contrast to this, in the experimental study in previous work [6], the leading edge shock wave was unsteady, which shows that a study on the particular mechanism which does not involve an unsteady incident shock would be compromised, since this means that there is significant additional unsteadiness from a different source in the experiment. A canonical experiment would therefore firstly require a reasonably steady incident shock wave in order to be comparable to the LES. Indeed, it is easier to generate a steady impinging shock wave if it is attached and oblique, at a high Mach number. Therefore, this type of shock wave is selected.

An oblique shock-wave/boundary-layer interaction on a curved surface at Mach 2.3 with a deflection angle of 24° from a shock generator is investigated. As expected, the interaction is strong, and the curvature causes an even larger separation bubble (Fig. 12) than for a flat plate (Fig. 13).

The increased separation caused by the curvature is not integral to the shock oscillation mechanism. As shown in Fig. 14, a similar oscillation mechanism is observed in both cases. The reason why the additional separation does not play an integral role in the behavior becomes clearer in Fig. 15. For the curved surface, much of the extended separation bubble remains during the downstream suppression phase, whereas in the flat plate case, the bulk of the separation bubble is suppressed.

Therefore, the curvature is neglected. Next, we examine additional factors that may influence the shock oscillation observed in experiment.

The thickness of the laminar boundary layer affects both the oscillation amplitude and frequency. This can be seen by comparing Fig. 14 (b) with Fig. 16 (a), which is at the same conditions as Fig. 14 (b) but with

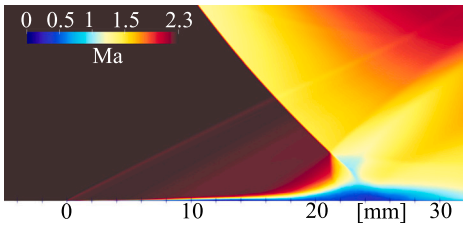

Fig. 13. Oblique SBLI on flat plate: Ma = 2.3, $\theta = 24^{\circ}$, time averaged Mach number contours.

Table 1
Grid resolutions for canonical configuration.

Mesh	Δx^+	wall Δy^+	Δz^+	far Δy^+	Cells
LES (low)	28	1	28	34	16M
LES (high)	14	1	14	34	40M
DNS	7	1	7	7	220M

a thicker oncoming boundary layer. A thicker boundary layer provides more space for the upstream influence to develop, leading to an increase in oscillation amplitude and a corresponding decrease in frequency due to the extended growth phase (Fig. 16(a)). Conversely, weaker shock strength results in less pronounced oscillations (Fig. 16(b)), and when the shock is too weak, the oscillation mechanism of interest becomes increasingly difficult to identify (Fig. 16(c)).

In experiments, additional noise is inevitable and has already been a challenge in previous studies (Nel et al., 2024 [6]). Weak interactions exacerbate this issue, making oscillations harder to detect and compromising the experiment. For this reason, a stronger interaction is preferable. In this case, the distance between the shock generator and the flat plate must be sufficient to ensure a straight incident shock wave, avoiding excessive influence from the expansion fan of the shock generator.

4. Shock oscillation mechanism in canonical research configuration

To examine the oscillation mechanism and the numerical requirements in greater detail, a sensitivity study is first conducted to assess the impact of mesh size and subgrid-scale modeling on the occurrence of the oscillation mechanism in the newly defined canonical case.

4.1. Numerical setup

This study focuses on the oblique SBLI domain (Fig. 17), representative of the canonical case. The simplicity of the domain allows for a direct comparison between two typical LES grid resolutions and a DNS-resolution grid. Relative to the separation bubble size, the domain width corresponds to approximately 10% of the chord in the spanwise direction, which might be considered a limitation of the current study based on computational limitations. Achieving DNS-level resolution for a grid-convergence comparison takes priority over matching the 20% chord-to-span ratio used in the cascade simulations. The grid sizes tested are summarized in Table 1, where the cell count of the DNS-resolution mesh is an order of magnitude greater than that of the coarser LES grid.

4.2. Results: mesh and subgrid-scale model sensitivity

To appreciate the complexity of the instantaneous flow field, it is shown in Fig. 18. Note the instabilities on the shear layer, which are transported in the upstream direction along with the upstream growth of the laminar separation.

First, we examine a time-enlarged view of the isentropic Mach number over time from the DNS-resolution solution (Fig. 19). The upstream-traveling separation shock is clearly visible, nearly vanishing as the

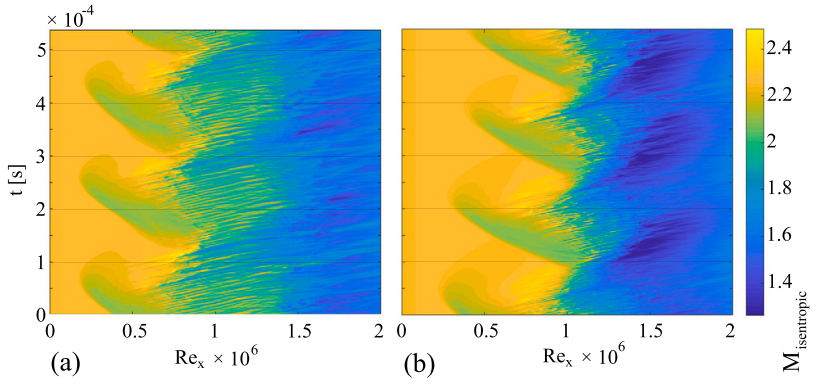

Fig. 14. Isentropic Mach number distribution with time on the wall for the curved surface case (left) and flat plate case (right) at Ma = 2.3, θ = 24°.

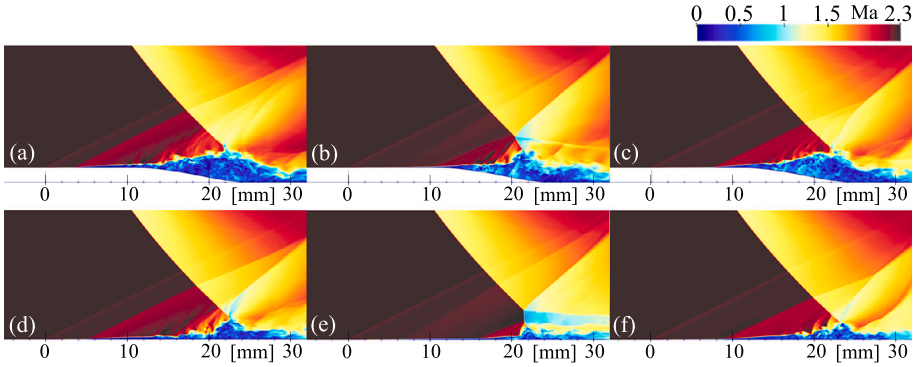

Fig. 15. Instantaneous Mach number contours for curved surface case (top) and flat plate case (bottom), with (a) and (d) showing the upstream phase of the oscillation, (b) and (e): downstream (collapsed) phase, (c) and (f): growth phase.

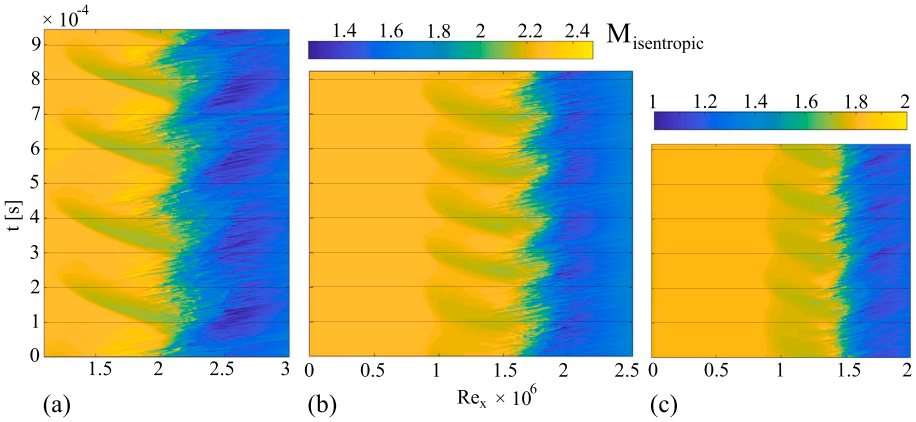

Fig. 16. Isentropic Mach number distribution with time on the wall for (a): thicker laminar boundary layer (note increased x Reynolds number compared to Fig. 15), Ma = 2.3, θ = 24°, (b): reduced shock strength case I (Ma = 2.3, θ = 13°) and (c): reduced shock strength case II (Ma = 1.7, θ = 11°).

laminar section collapses. Additionally, instabilities are observed being transported upstream, and during the collapse of the separation bubble, these instabilities retreat at a speed roughly twice as fast as their upstream transport during the growth phase. Notably, the separation bubble collapses more rapidly than it grows. Furthermore, while the oscillation is not perfectly periodic, a distinct periodic pattern is evident.

In Fig. 20, the full solution can be seen for the DNS-resolution grid. This solution is compared to LES simulations using the SIGMA [21] and WALE [22] subgrid scale models as well as no-model on the LES grids. The Smagorinsky SGS model [23], which has previously shown excessive smearing at the SBLI [6], had lead to a divergence of the computational setup, due to growth of the separation bubble over the leading edge.

A precise comparison of shock oscillation dynamics would require simulating hundreds of oscillation cycles, which would be highly resource-intensive. To address this, we limit the simulation duration, stopping the oscillation once the standard error of the average Mach number contours drops below a threshold of just over 0.85% of the free-stream Mach number (Fig. 21).

Fig. 23 shows the difference in Mach number between LES on the high and low resolution grids (introduced in Table 1) compared to the DNS-resolution solution. As one would expect, the no-model LES on the coarse grid (Fig. 23a) performs the worst in terms of the difference between the average Mach number contours to the DNS-resolution solution. One can also see from the isentropic Mach number results over time, that the no-model LES on the coarse grid (Appendix: Fig. A.47)

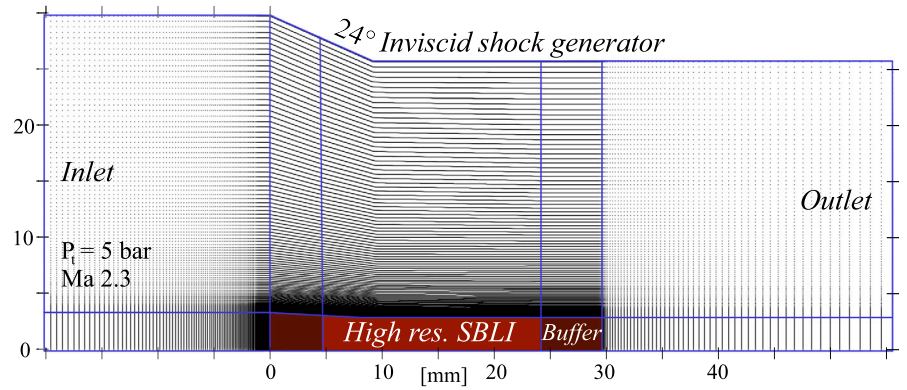

Fig. 17. Canonical setup computational domain showing zone where the SBLI is captured in high resolution.

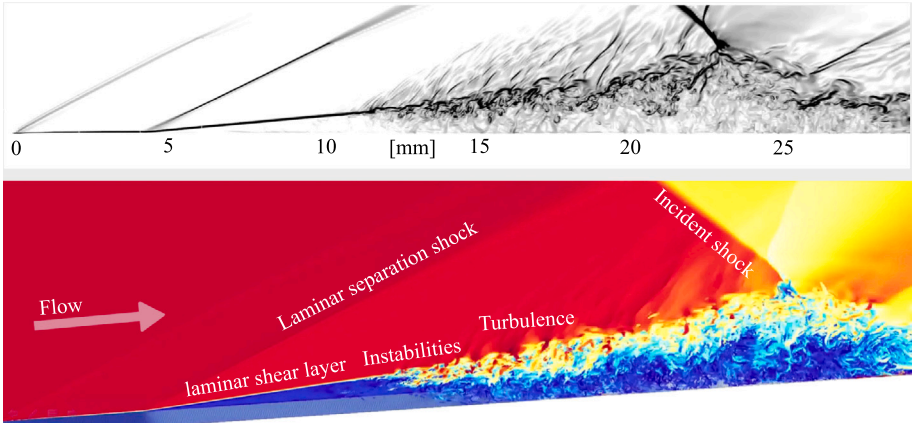

Fig. 18. Instantaneous view of DNS solution with mid-plane contours of $|\nabla\rho|/\rho$ on the top, and Mach number contours supported by lambda-2 ISO surfaces to show turbulent structures.

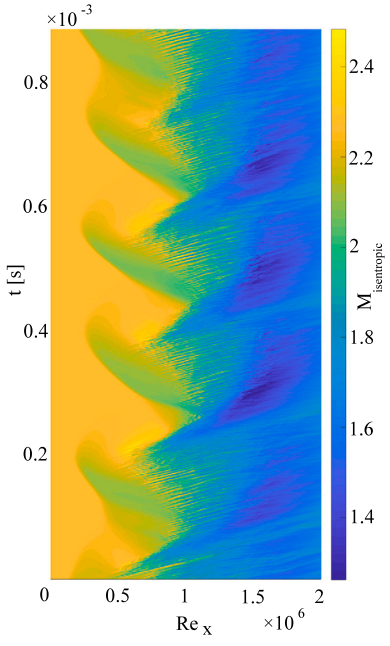

Fig. 19. DNS-resolution solution with Y-axis zoomed to get a clear view of the pattern.

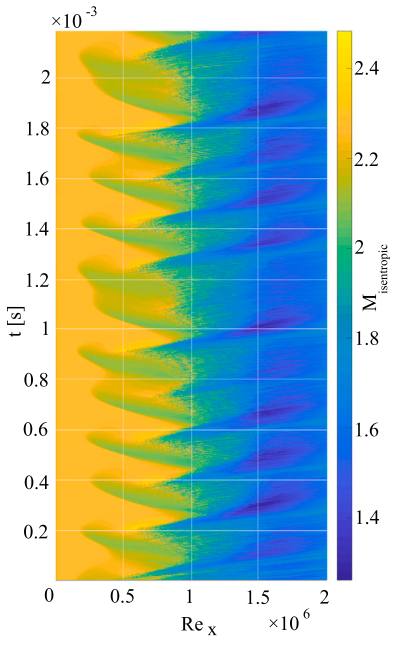

Fig. 20. Full DNS-resolution solution: isentropic Mach number distribution with time.

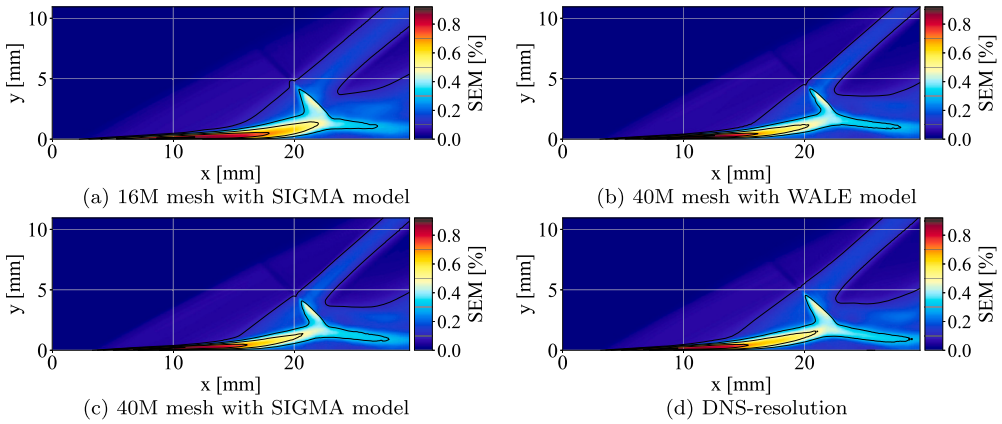

Fig. 21. Standard error of the mean Mach number normalized by the free stream Mach number for different grid / SGS solutions.

shows a tendency for the upstream laminar section of the separation bubble to collapse prematurely when compared to the DNS-resolution grid, which does not show such a premature collapse for the resolved cycles. Such premature collapses also appear in the WALE (Appendix: Fig. A.48) and SIGMA (Appendix: Fig. A.49) models at the low resolution grid, although the overall solution is better in terms of average Mach number, for example shown through the difference in average Mach number between the SIGMA 16M-grid case and the DNS-resolution solution in Fig. 23b. In Sect. 5, we will see that the premature collapse does not appear in the experiment, and therefore the preliminary comparison between numerical and experimental results suggest that this is a non-physical artifact (likely occurring from the differences in the shear layer instabilities and turbulence) due to the low resolution grid.

Regarding the characteristics of the averaged flow field (Fig. 22), particularly the size of the separation bubble, the 40M-grid with SIGMA and WALE models show good agreement with the DNS-resolution solution, offering better accuracy than the coarse grid with SGS models. This is also evident from the differences illustrated in Figs. 23c and 23d, from which the improved representation of the fine grid using WALE and SIGMA models, to the DNS-resolution flow field relative to the coarse grid can be seen. The shear layer is a region showing larger differences to the DNS-resolution solution, with differences of up to $\Delta Ma = 0.2$ for the high resolution (40M mesh), $\Delta Ma = 0.62$ for the low resolution (16M) mesh with subgrid-scale model, and over $\Delta Ma = 0.9$ for the no-model LES at low resolution. Note that there is little difference between the WALE and SIGMA models (Fig. 24) in terms of average Mach number. To further analyze differences between the solutions, we return to the dynamics and examine RMS Mach number fluctuations.

The RMS Mach number fluctuations are shown in Fig. 25, focusing on the higher resolution results. The results suggest a slightly better agreement between the SIGMA and DNS-resolution solutions when compared to the WALE solution. Notably, the fluctuations just above the section of the separation bubble downstream of the maximum separation height show a better agreement for the SIGMA model. This can be seen more clearly in a wall-parallel cut at $y = 2.8$ mm (Fig. 26a). Furthermore, the maximum RMS Mach fluctuation in the shear layer is also slightly closer for the SIGMA model (Fig. 26b).

The isentropic Mach number distributions in time for the 40M-grid with WALE (Fig. 27) and SIGMA (Fig. 28) SGS models exhibit closer time-dependent behavior to the DNS-resolution solution than the 16M grid, in that no early laminar separation bubble collapse is seen. Although differences in features between the WALE and SIGMA subgrid-scale model isentropic Mach number distributions in time are not clearly noticeable, we note that when ignoring the occasional merged peaks for all the solutions, the DNS-resolution solution (Fig. 20) exhibits a "sharper" footprint at the upstream position, with the laminar separation persisting for a slightly shorter duration at its maximum compared

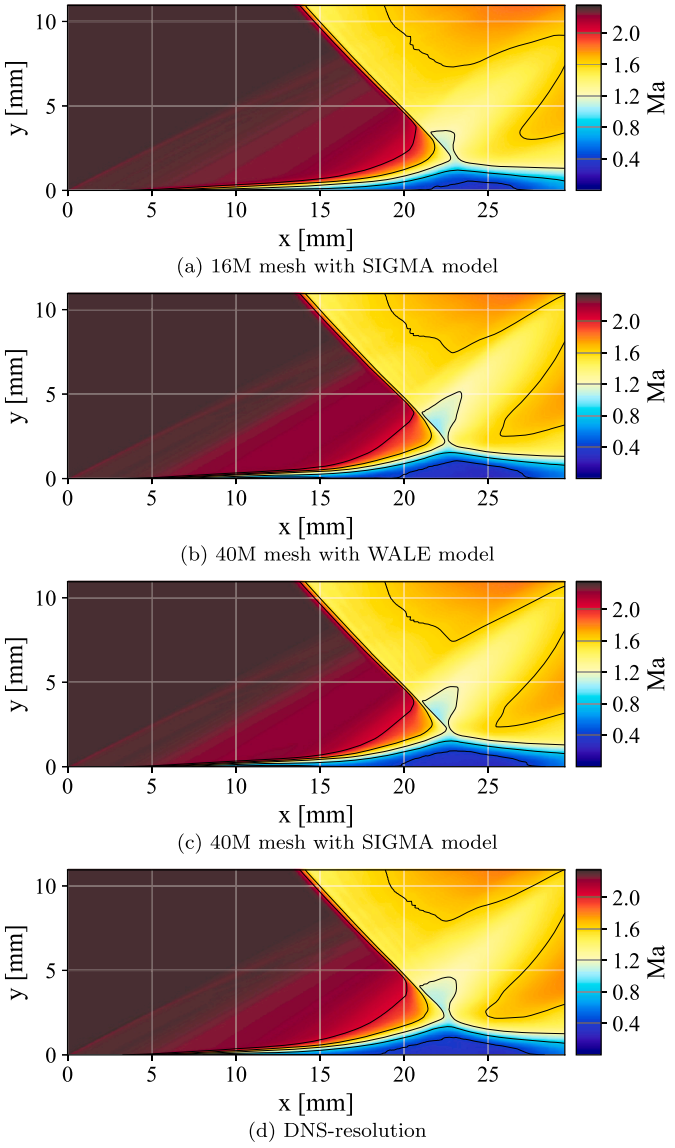

Fig. 22. Average Mach number distribution across various mesh resolutions and subgrid-scale models.

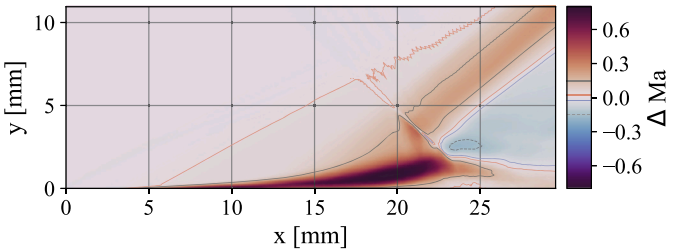

(a) 16M no-model LES mesh vs. DNS-resolution

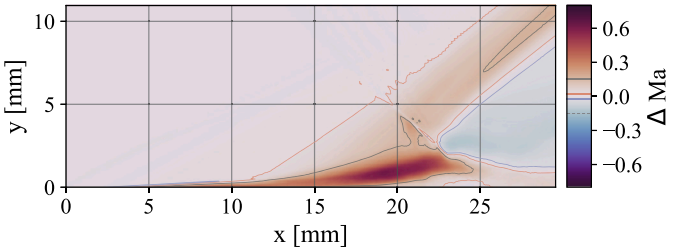

(b) 16M mesh SIGMA vs. DNS-resolution

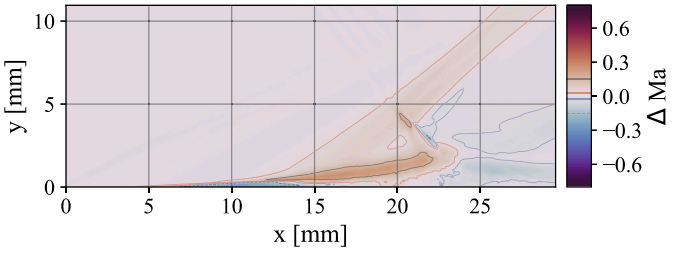

(c) 40M mesh WALE vs. DNS-resolution

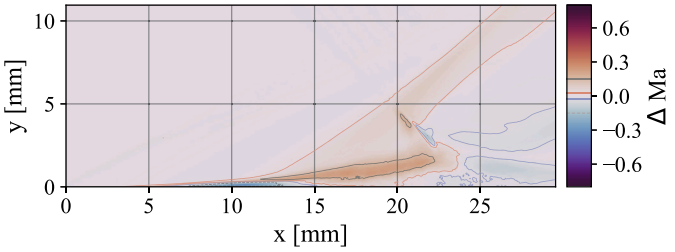

(d) 40M mesh SIGMA vs. DNS-resolution

Fig. 23. Comparison of Mach number differences across various mesh resolutions with DNS-resolution solution subtracted from the various cases.

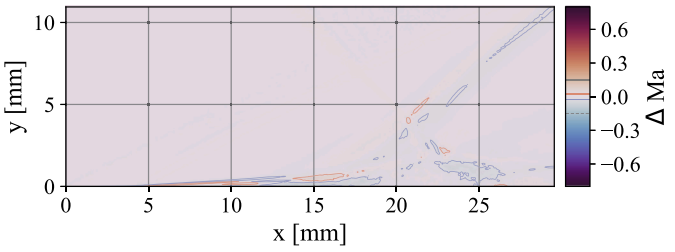

Fig. 24. Canonical configuration average Mach number distribution: 40M WALE solution subtracted from 40M SIGMA solution.

to the 40M-grid solutions. This naturally facilitates a mechanism for a frequency discrepancy.

Using wall-parallel Mach number cuts in time, the dynamic behavior for the fine LES grid solutions (Fig. 29 and 30) and the DNS-resolution grid (Fig. 31) is shown. There is a qualitative difference in the upstream turbulent peak shapes of the cut at 1.05 mm (subfigures (b) of Figs. 29 to 31), in that the DNS-resolution solution has sharper, more abrupt turbulent peaks at the separation in time for each oscillation cycle. This is also leaves a signature on the higher wall-parallel cuts of the DNS-resolution

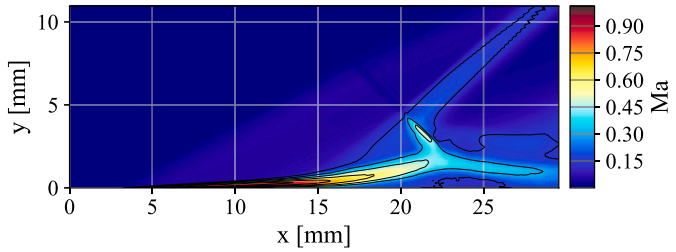

(a) 40M mesh with WALE model

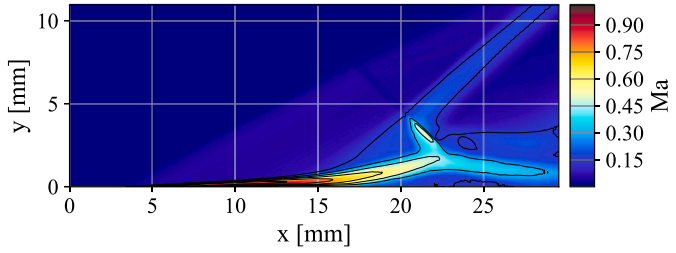

(b) 40M mesh with SIGMA model

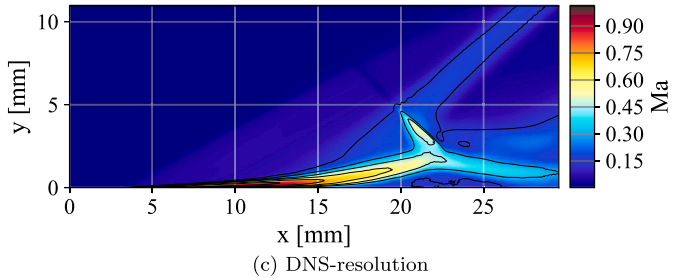

(c) DNS-resolution

Fig. 25. RMS Mach number fluctuations across different mesh resolutions and turbulence models. Subfigures (a) and (b) show the RMS Mach fluctuations for 16M and 40M meshes with the SIGMA model, respectively, while subfigure (c) provides a reference at DNS-resolution.

solution in Figs. 31 (c) and (d), in that the compression waves arising from the sharper turbulent separation extend upstream of x = 15 mm for Fig. 31, contrary to the 40M-grid solutions in Figs. 29 and 30. Furthermore, comparing the DNS resolution solution Fig. 31 (c) to the 40M-grid solutions in Figs. 29 (c) and 29 (c), we note that the DNS-resolution solution shows a slightly more severe separation bubble height at the end of each oscillation cycle than the 40M-grid solutions. Overall, the results suggest that a sensitivity of the oscillation to the numerical setup remains at the fine grid. Nevertheless, the results show that the oscillation mechanism can be resolved with a particular accuracy using such a grid resolution, which has 5.5 times less cells. For further calculations, such as for a tripped configuration, we therefore choose the SIGMA subgrid-scale model on the 40 million-cell grid.

4.3. Shear layer instabilities

To investigate the source of upstream-generated turbulence and near-wall behavior, we analyze a wall-parallel cut at 0.35 mm above the wall. This cut intersects the laminar shear layer during the upstream growth phase and captures turbulence from the separation region which drops below 0.35 mm during the collapse phase. Fig. 32 illustrates this through the velocity magnitude fluctuations relative to the mean flow.

For the same cut, static pressure fluctuations are presented in Fig. 33, where downstream-advecting pressure fluctuations from Kelvin-Helmholtz (K-H) instabilities on the shear layer can be seen emanating from the shear layer area (Fig. 33). Upstream propagating z-velocity waves induced by the flapping of K-H instabilities which propagate upstream with the growth of the laminar part of the separation, can be seen in Fig. 34.

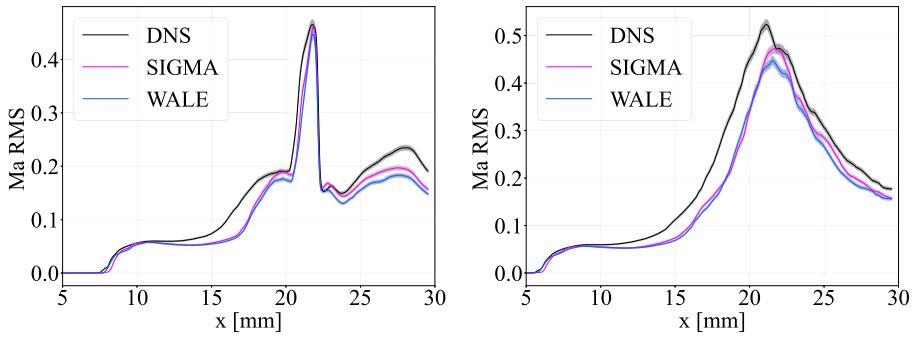

(a) RMS Mach number fluctuations at wall-parallel cut above separation (y=2.8 mm).

(b) RMS Mach number fluctuations at wall-parallel cut through shear layer (y=1.7 mm).

Fig. 26. 40M grid vs. DNS-resolution: comparison of RMS Mach number fluctuations with shaded statistical uncertainty at two wall-parallel cuts.

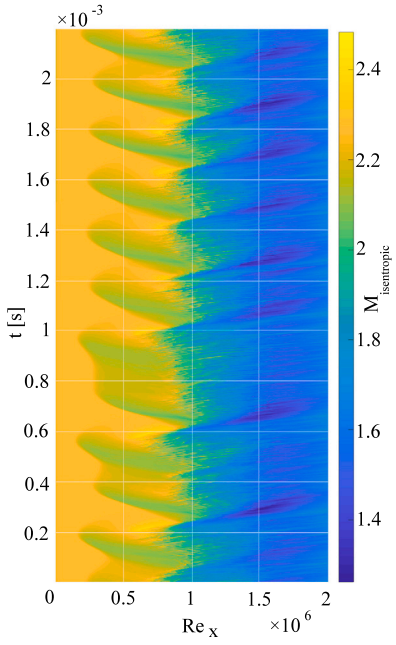

Fig. 27. WALE LES (40M-grid) solution: isentropic Mach number distribution with time.

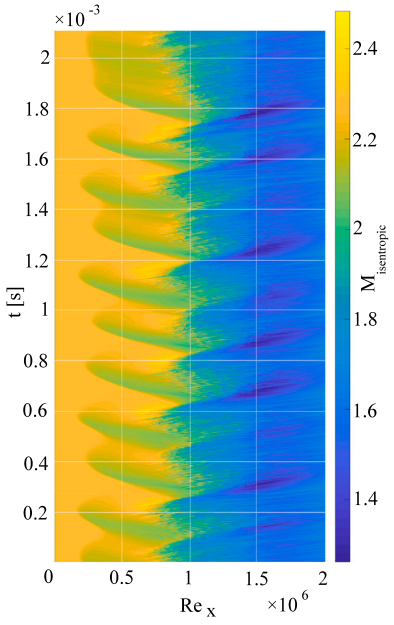

Fig. 28. SIGMA LES (40M-grid) solution: isentropic Mach number distribution with time.

Additionally, as also noted in the isentropic Mach number distribution plots, we observe the shifting transition location. This feature, along with the laminar separation shock, serves as a key aspect for experimental validation of the mechanism, which is being addressed in concurrent work [15].

4.4. Turbulent boundary layer case

It was shown by Nel et al. [6] that the described oscillation mechanism on the highly loaded transonic cascade ceases when the boundary layer is turbulent. To demonstrate this for the canonical research configuration, step elements (0.125 mm × 0.125 mm × 0.175 mm, z-spacing 0.175 mm) are applied 4.6 mm from the leading edge of the flat plate in order to create a turbulent boundary layer upstream of the SBLI. Instantaneous snapshots showing the oncoming turbulent boundary layer, step location and SBLI region, are shown in Fig. 35. The time-averaged Mach number contours in Fig. 36 show a significantly reduced separation, a Mach stem feature and a distinct reflected shock wave. Furthermore, the upstream influence of the SBLI is greatly reduced in comparison to the laminar case, attributed to the absence of a periodically growing laminar separation shock. The RMS Mach number fluctuations are shown in Fig. 37. The stabilizing effect of the turbulent oncoming boundary layer can be seen, with greatly reduced fluctuations in comparison to the laminar case. The highest fluctuations occur in the Mach stem region, whereas the highest fluctuations for the laminar case appear in the upstream section of the separation. Wall-parallel cuts of Mach number contours show the temporal behavior (Fig. 38) and the significantly reduced motion when compared to the same cuts in the laminar case (Fig. 30). Nel et al. [15] experimentally investigated the difference in shock oscillation frequency spectra obtained between turbulent and laminar configurations for the experiment realized from the present work.

5. Qualitative experimental comparison

To show the consistency in behavior between the shock oscillation mechanism of the derived canonical research configuration showing the same type of oscillation mechanism as the cascade, to that of the realized canonical experiment [15], we present data of Nel et al. [15] through wall-parallel cuts of Schlieren intensity in time. This way, the qualitative match between separation shock and separated shear layer behavior of the experiment vs. canonical research configuration can be observed. The Mach number in both experiment and current numerical setup is 2.3. The practical implications of the experiment caused a deviation from the current geometry and Reynolds number of the current numerical setup. At the shock impingement location, Reynolds num-

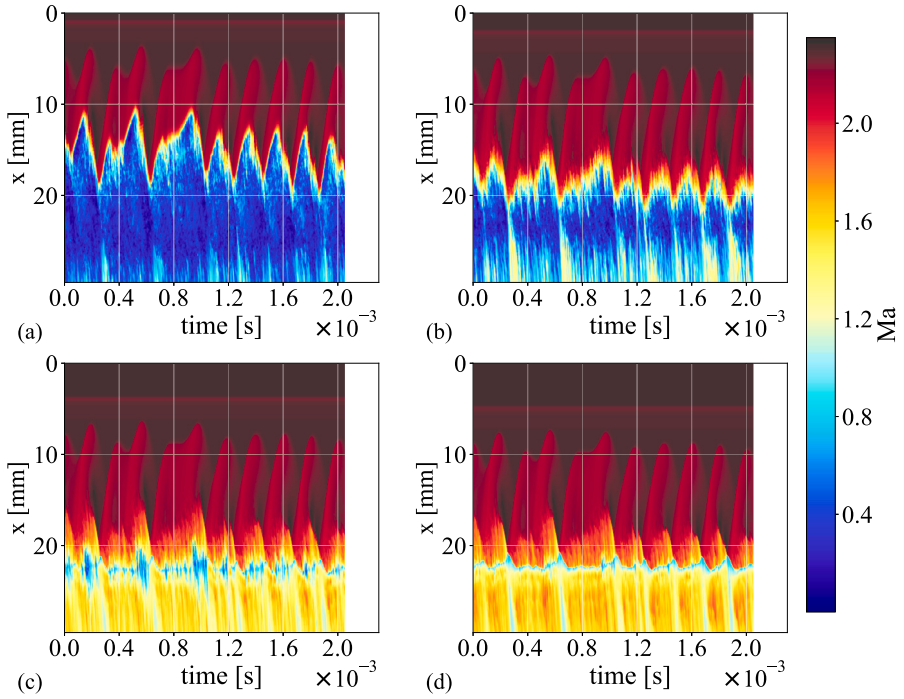

Fig. 29. Canonical configuration WALE 40M LES: streamwise cuts at (a) 0.5 mm, (b) 1.05 mm, (c) 1.93 mm and (d) 2.45 mm above the wall.

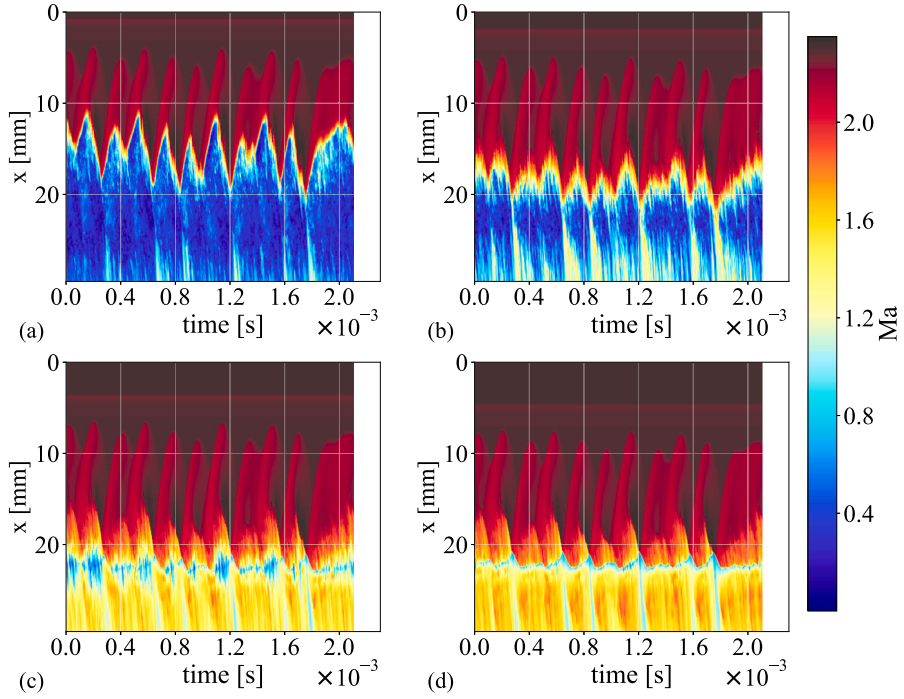

Fig. 30. Canonical configuration SIGMA 40M LES: streamwise cuts at (a) 0.5 mm, (b) 1.05 mm, (c) 1.93 mm and (d) 2.45 mm above the wall.

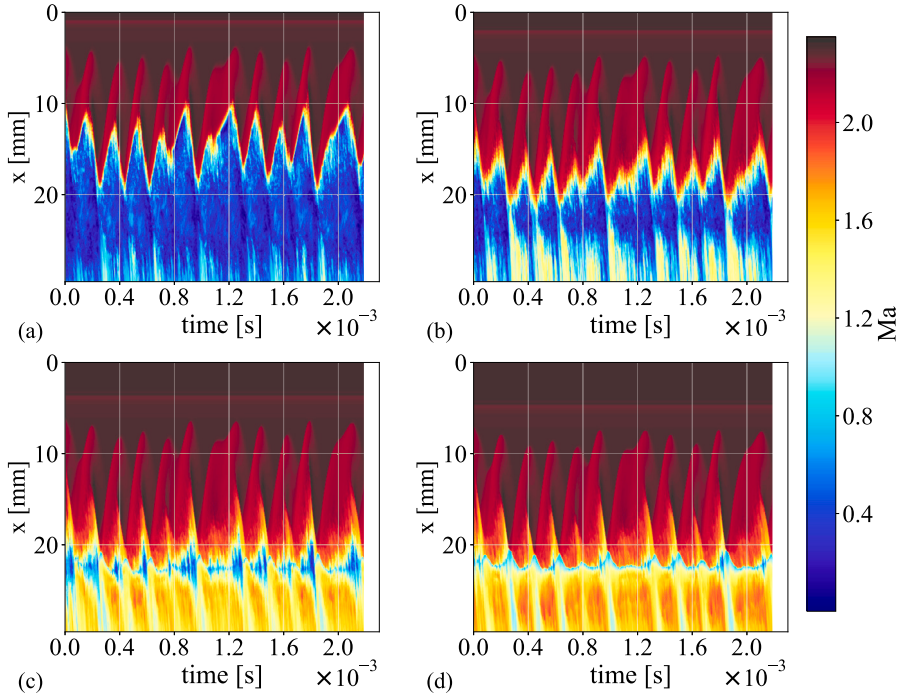

Fig. 31. Canonical configuration DNS-resolution: streamwise cuts at (a) 0.5 mm, (b) 1.05 mm, (c) 1.93 mm and (d) 2.45 mm above the wall.

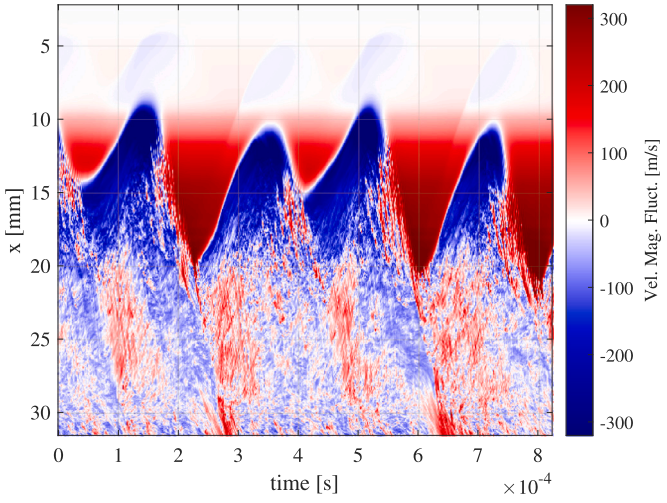

Fig. 32. Canonical configuration SIGMA 40M LES: velocity fluctuations from mean at $y = 0.35$ mm wall-parallel cut.

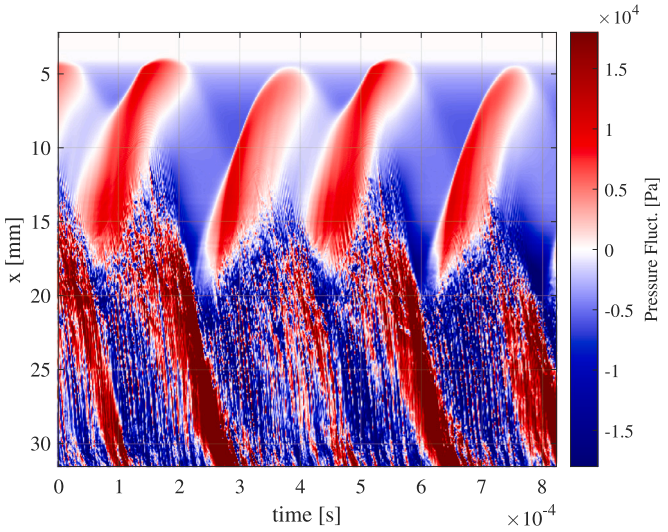

Fig. 33. Canonical configuration SIGMA 40M LES: Static pressure fluctuations from mean at $y = 0.35$ mm wall-parallel cut.

ber of the experiment is 3.28E6, whereas for the numerical setup used in the previous section, it is 1.6E6. The difference in Reynolds number can have an effect on the shock oscillation frequency and extent of the upstream growth phase of the oscillation, as already shown when comparing Fig. 16 (a) to Fig. 15 (b). Therefore, we perform a qualitative comparison in the present work. For a quantitative comparison of the frequencies observed in numerical simulations and experiments at matching Reynolds numbers, the reader is referred to Nel et al. [14,15], where quantitative analyses (dynamic mode decomposition spectra and spatial modal studies) are presented based on a setup derived from the present work. A characteristic length scale is introduced in Nel et al. [15], based on the upstream travel distance of the laminar separation shock before the laminar separation collapses. This characteristic length scale leads to matching Strouhal numbers between the experiment and simulation. Spark light shadowgraphy was employed to identify the transition location on the upstream separated shear layer, confirming the onset of transition through Kelvin–Helmholtz instabilities [15].

The experimental setup in the TST-27 blowdown wind tunnel of the Delft University of Technology is shown in Fig. 39. The details of the experimental setup, geometry, and analyzed experimental flow field have been reported [15,14]. High-speed Schlieren imaging (Photron FASTCAM NOVA S12, 100 kHz, 384 × 240 pixels, exposure time 1/300 000 s) is employed in a z-type Schlieren setup.

5.1. Laminar oncoming boundary layer

Several wall-parallel locations are introduced from which to show the Schlieren intensity profiles plotted over time. These locations can be seen in the time averaged Schlieren intensity representation of Fig. 40.

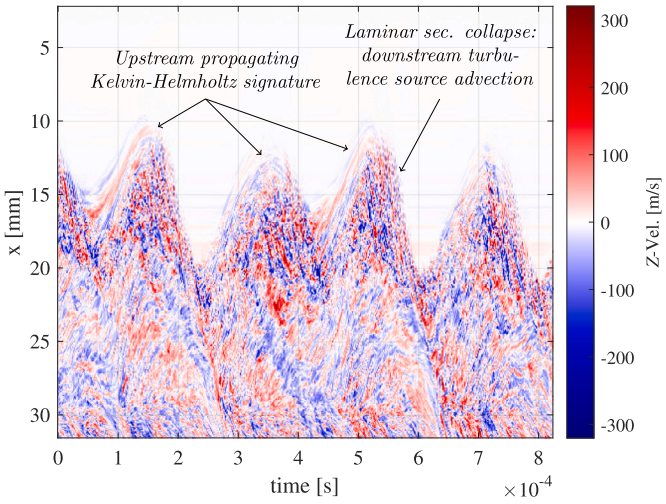

Fig. 34. Canonical configuration SIGMA 40M LES: z-velocity fluctuations at $y = 0.35$ mm wall-parallel cut.

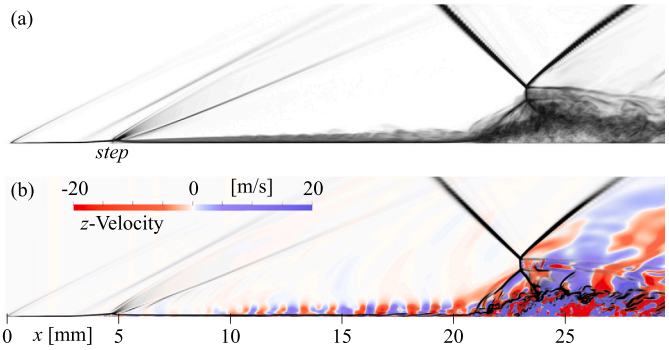

Fig. 35. Canonical configuration SIGMA 40M: instantaneous snapshots showing turbulent oncoming boundary layer. (a): volumetric numerical shadowgraph. (b): z-Velocity fluctuations at mid-plane section, with superimposed mid-plane numerical shadowgraph.

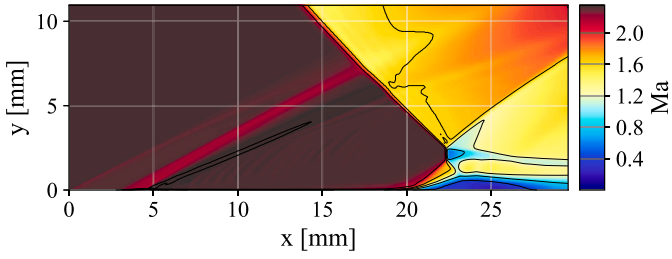

Fig. 36. Canonical configuration (SIGMA SGS model, 40M grid) turbulent boundary layer: Time-averaged Mach number contours.

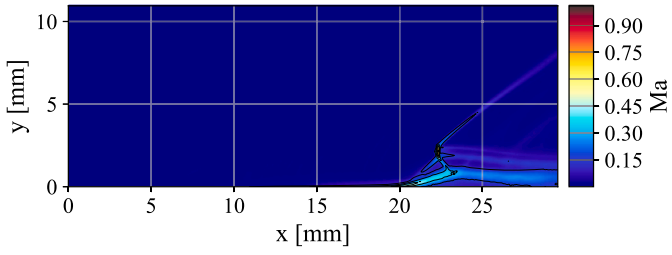

Fig. 37. Canonical configuration (SIGMA SGS model, 40M grid) turbulent boundary layer: RMS Mach number fluctuations.

The behavior of the laminar separation shock in the experiment can be seen in the $y = 0.7$ mm wall-parallel cut with vertical knife edge for the Schlieren setup (Fig. 41). Similar to what was seen in the cascade and canonical configurations, the laminar separation shock (between $x = 10$ mm and 22 mm) travels upstream with a pronounced trajectory, as the flow deflection from a steeper separation causes a stronger separation shock during the upstream propagating phase. As the laminar separation collapses, the signature of the retreating separation is less pronounced due to collapsing in a near wall-tangential fashion. Notably, the premature shear layer collapse which was observed for the low resolution LES meshes, is not observed, with the behavior more closely resembling the DNS-resolution or high-resolution LES simulations. Furthermore, the periodically increased turbulence resulting from the oscillation and affecting the bulk separation, appears as streaks in the turbulent downstream region (beyond $x = 40$ mm), qualitatively analogous to the downstream turbulent streak-like effects seen in the numerical results involving pressure effects (e.g. Figs. 33 and 28).

A shadowgraph (no knife edge) setting for the Schlieren setup reveals the upper shear layer behavior in a wall-parallel cut at $y = 0.50$ mm (Fig. 42). Here, the shear layer behavior which can be seen around $x = 20$ mm is analogous to cutting through the shear layer in the numerical Mach number plots of e.g. Fig. 31 (a).

Although the Schlieren setting with vertical knife edge is satisfactory for showing the laminar separation shock, the downstream region around the separation shock waves from turbulent thickening of the shear layer is somewhat over-saturated. Therefore we use the shadowgraph setting to show time dynamics both laminar and turbulent separation shocks in the same plot (Fig. 43). From this figure, the turbulent separation shock existing briefly during the collapse of the laminar separation can be seen in the wall-parallel cut at $y = 1.2$ mm. In a concurrent study [15], spark light shadowgraphs showing shear layer instabilities support the finding of the flow field exhibiting a downstream position of transition after the laminar section collapse and the flow field briefly exhibiting a single (turbulent) separation shock, since the instabilities from the collapse advect downstream. In the next subsection, the cut at $y = 23.8$ mm is used to compare the reflected shock behavior of the laminar and turbulent configurations.

5.2. Turbulent oncoming boundary layer

Next, we examine the turbulent boundary layer case, for which the time averaged Schlieren intensity map with interrogation lines can be seen in Fig. 44.

In order to promote transition, a step of 0.1 mm×1.3 mm is applied 3 mm from the leading edge. As noted by Nel et al. [15] who employed dynamic mode decomposition, the shock is stabilized by introducing a turbulent boundary layer (Fig. 45). The stabilizing effect on time dynamics can be seen in Fig. 46. A single (turbulent) separation shock persists. From the Schlieren image, one can already note the more distinct separated shear layer, separation- and reflected shock waves when comparing the turbulent boundary layer case (Fig. 44) to the laminar boundary case (Fig. 40). This indicates a stabilization, which we further demonstrate through wall-parallel Schlieren intensity plots in time.

The stabilizing effect on the reflected shock can be seen in the comparison of laminar and turbulent cases (wall-parallel cut at $y = 23.8$ mm) in Fig. 46. The higher frequency oscillation induced by the laminar SBLI shock oscillation mechanism at 3748 Hz [15] is eliminated.

6. Conclusions

In the current study, we demonstrated the equivalence of the shock oscillation type observed in Large Eddy Simulations (LES) of a highly loaded transonic cascade and a canonical research configuration which can be studied in a practical experiment. Subsequently we showed the equivalence of the observed mechanism in the realized experimental

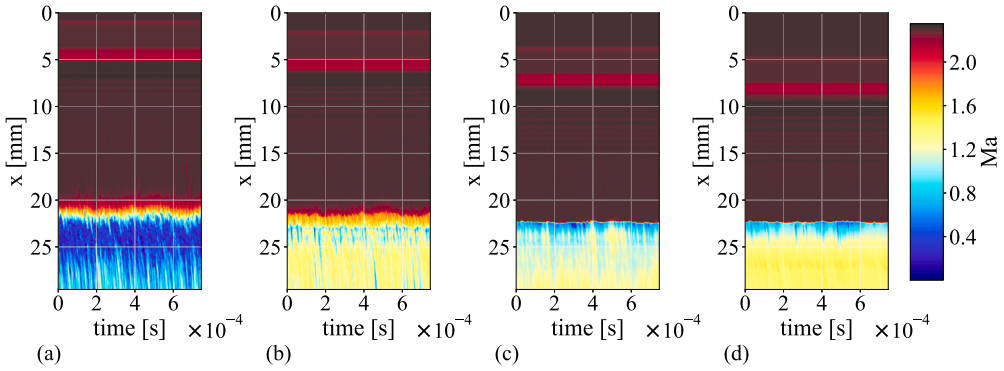

Fig. 38. Canonical configuration (SIGMA SGS model, 40M grid) turbulent boundary layer: streamwise cuts at (a) 0.5 mm, (b) 1.05 mm, (c) 1.93 mm and (d) 2.45 mm above the wall.

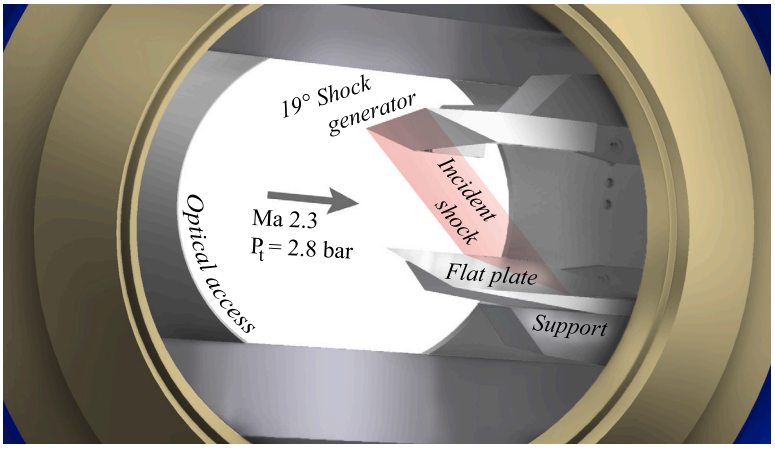

Fig. 39. Rendering of experimental setup realized at TU Delft.

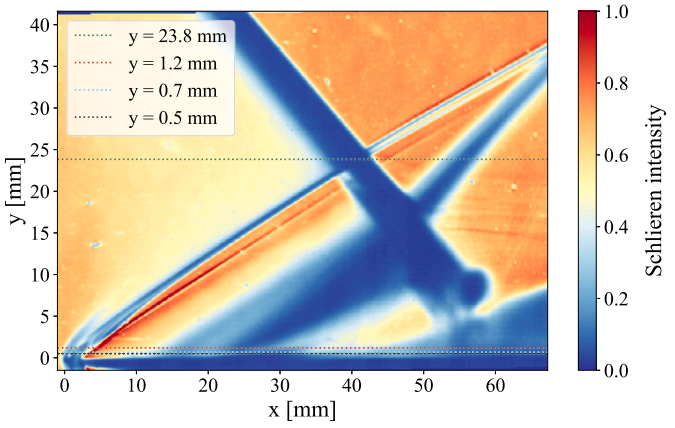

Fig. 40. Averaged high-speed Schlieren (vertical knife edge) for the laminar boundary layer case.

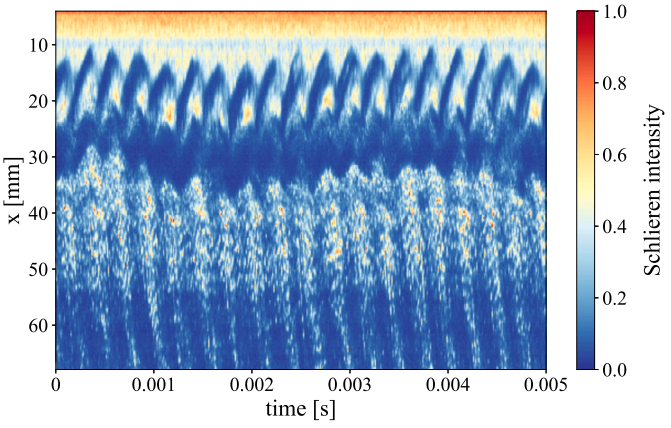

Fig. 41. Wall-parallel Schlieren (vertical knife edge) intensity profile for the laminar boundary layer case at a height of 0.7 mm.

research configuration, and that this mechanism is eliminated when tripping the boundary layer in both the experiment and LES cases. Notably, the pronounced signature of the upstream growth phase of the laminar section of the separation bubble, through a steeper deflection angle of the upstream laminar separation, can be noticed in all laminar cases, showing a matching behavior of the shock oscillation mechanism. The shock oscillation features a periodically collapsing separation bubble with Kelvin–Helmholtz instabilities on the shear layer upstream of the shock. This separation bubble grows in the upstream direction, pulling the instabilities with it in front of the shock wave. At a far enough upstream position, the turbulence from these instabilities is significant enough to wash away (or suppress) a significant part of the separation bubble, especially the upstream laminar section, at which stage the turbulence is no longer generated upstream of the shock and the separation bubble can start to grow again. The upstream growth is highlighted by the formation of a secondary separation shock. If the boundary layer exhibits significant upstream disturbances, such as in the presence of a tripping device, the oscillation amplitude is significantly reduced compared to the laminar case. This is because the shock oscillation mechanism described cannot exist when the boundary layer is turbulent or when instabilities lead to transition too early on the separated shear layer.

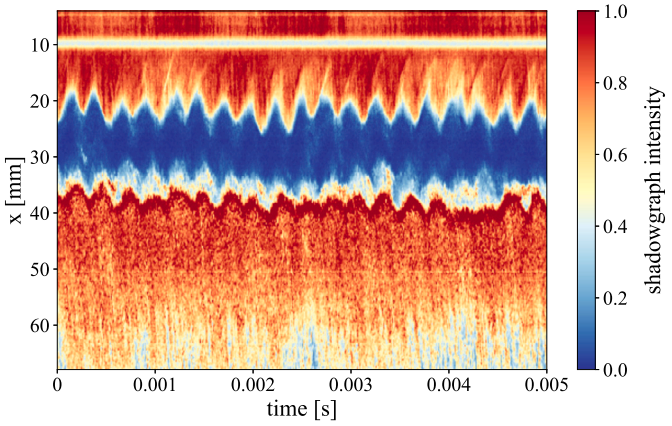

Fig. 42. Wall-parallel Schlieren intensity profile for the laminar boundary layer case at a height of 0.5 mm. Optical artifact at $x = 10$ mm.

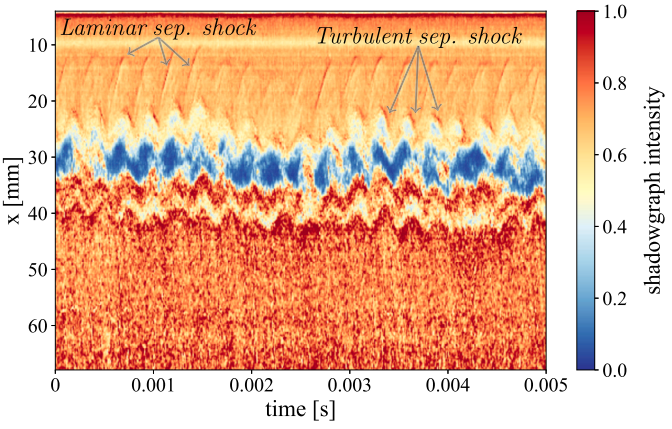

Fig. 43. Wall-parallel shadowgraph intensity profile for the laminar boundary layer case at a height of 1.2 mm.

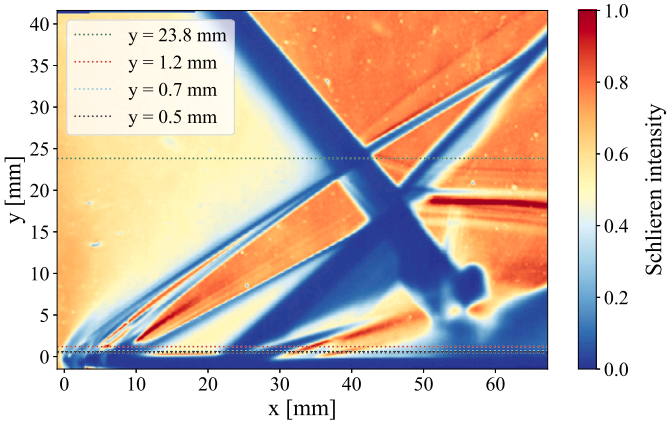

Fig. 44. Averaged high-speed Schlieren for the tripped boundary layer case.

Pressure fluctuations could be seen emanating from a region on the shear layer where structured, upstream-propagating z-velocity fluctuations were observed, indicative of an upstream propagating Kelvin-Helmholtz instability.

With a considerable computational advantage- requiring 5.5 times fewer cells than the DNS-resolution solution, the high-resolution LES simulations (40 million grid points) demonstrated good agreement, with the largest average Mach number discrepancies observed in the shear layer ($\Delta Ma = 0.2$). Particularly, a significant improvement in the separation bubble size was observed when compared to the lower (16 million

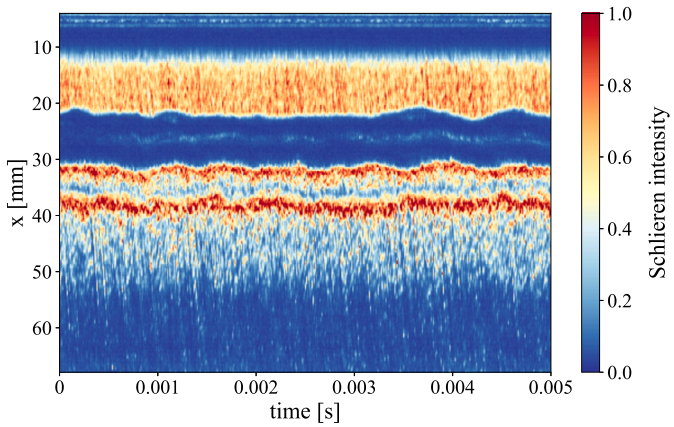

Fig. 45. Wall-parallel Schlieren intensity profile over time for the tripped boundary layer case at a height of 0.7 mm.

cells) resolution mesh. The dynamic behavior of the high-resolution grid closely resembled the DNS-resolution solution, as it did not exhibit the premature collapse of the upstream laminar section observed in low-resolution cases. Experimental results supported this finding, suggesting that the premature collapse leading to more chaotic behavior is non-physical, as the experiment also exhibited cleaner periodic oscillations without such early collapses. Although the differences between the SIGMA and WALE models with regard to the time-averaged Mach number are not significant, the RMS Mach number fluctuations of the SIGMA solution more closely resembles the DNS-resolution solution.

The brief existence of a turbulent separation shock immediately after the laminar separation reaches a maximum upstream position (initial collapse state) could be confirmed using high speed shadowgraphs.

A stabilization of the oscillation for the canonical research configuration with a turbulent oncoming boundary layer could be demonstrated both experimentally and numerically, with the stabilization in the numerical case being more significant due to the idealized conditions, but with both cases showing the absence of the otherwise large scale movement accompanied by a secondary (laminar) separation shock for a laminar oncoming boundary layer.

The study served as the link between the canonical research configuration and the highly loaded transonic cascade shock oscillation mechanism observations, and additionally serves a basis for defining numerical requirements. The study can be used to calculate the cost of resolving the particular shock oscillation mechanism on full-span fan applications and subsequently design the surface finish or geometry in a way that suppresses the source. Furthermore, the study provides engineers with insights into the sources of shock oscillation that can arise in transonic fan applications. Future studies should include a project dedicated to detailed, long running LES for in-depth quantification of the differences in dynamics between different subgrid scale models. In that case, a sensitivity study to grid sizes, anisotropy in the grid, and subgrid-scale modeling parameters would aid in understanding optimal numerical requirements for the specific shock oscillation mechanism, for which the current study provides the foundation.

CRediT authorship contribution statement

Philipp L. Nel: Writing – original draft, Visualization, Validation, Methodology, Investigation, Formal analysis, Conceptualization. **Anne-Marie Schreyer:** Writing – review & editing, Supervision. **Ferry F.J. Schrijer:** Supervision, Resources. **Bas W. van Oudheusden:** Resources. **Marius Swoboda:** Resources, Funding acquisition.

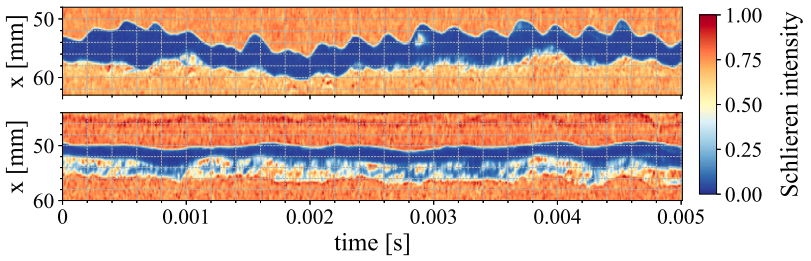

Fig. 46. Wall-parallel Schlieren intensity profile over time extracted for the laminar (top) and tripped cases (bottom) at the reflected shock ($y = 23.8$ mm).

Declaration of competing interest

The authors declare the following financial interests/personal relationships which may be considered as potential competing interests: Philipp Nel reports financial support was provided by European Commission. If there are other authors, they declare that they have no known competing financial interests or personal relationships that could have appeared to influence the work reported in this paper.

Acknowledgements

The author participated in the TEAMAero project, which has received funding from the European Union's Horizon 2020 research and innovation programme under grant agreement No 860909.

Appendix A. Coarse grid LES isentropic Mach distributions

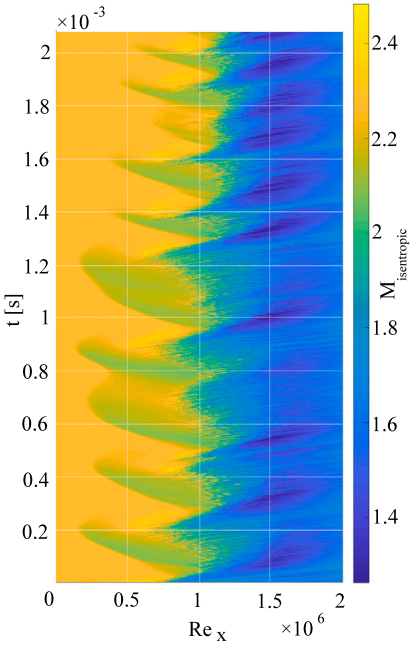

Fig. A.47. No-model LES (16M grid) solution: isentropic Mach number distribution with time.

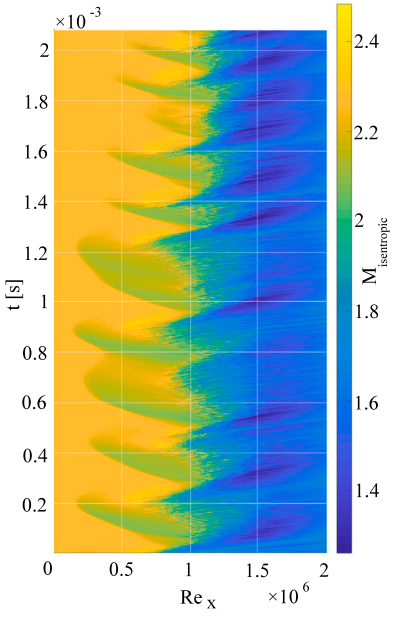

Fig. A.48. WALE LES (16M grid) solution: isentropic Mach number distribution with time.

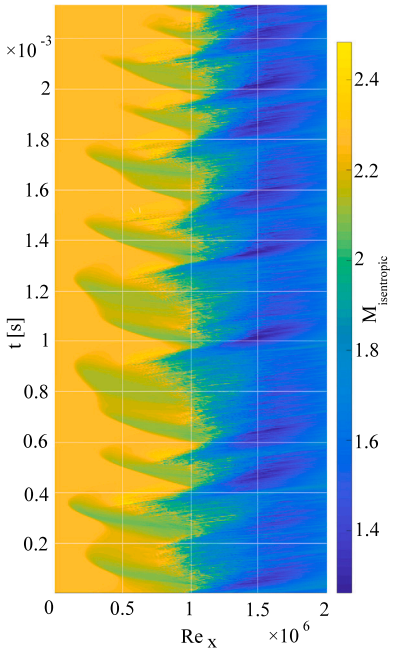

Fig. A.49. SIGMA LES (16M grid) solution: isentropic Mach number distribution with time.

Data availability

The authors do not have permission to share data.

References

[1] Patrick Grothe, et al., Internal flows—compressors, in: Piotr Doerffer, et al. (Eds.), Transition Location Effect on Shock Wave Boundary Layer Interaction: Experimental and Numerical Findings from the TFAST Project, Springer, Cham, Switzerland, 2021, pp. 229–296.

[2] Role of shock and boundary layer separation on unsteady aerodynamic characteristics of oscillating transonic cascade, in: Volume 4: Turbo Expo 2003. Turbo Expo: Power for Land, Sea, and Air, June 2003, pp. 349–356.

[3] Alexander Hergt, et al., The present challenge of transonic compressor blade design, J. Turbomach. (ISSN 0889-504X) 141 (9) (May 2019) 091004, https://doi.org/10.1115/1.4043329.

[4] Jyoti Ranjan Majhi, Kartik Venkatraman, Numerical simulation of transonic buffet in an axial-flow fan, in: AIAA AVIATION 2023 Forum, 2023.

[5] The effects of lean and sweep on transonic fan performance, in: Volume 5: Turbo Expo 2002, Parts A and B. Turbo Expo: Power for Land, Sea, and Air, June 2002, pp. 23–32.

[6] Philipp L. Nel, et al., Effect of transition on self-sustained shock oscillations in highly loaded transonic rotors, AIAA J. 62 (6) (2024) 2063–2075, https://doi.org/10.2514/1.J063378.

[7] A. Gomar-N, G. Gourdain, Guillaume Dufour, High-Fidelity Simulation of the Turbulent Flowin: A Transonic Axial Compressor, vol. 1, Jan. 2011.

[8] Chunill Hah, Large eddy simulation of transonic flow field in NASA Rotor 37, in: 47th AIAA Aerospace Sciences Meeting Including the New Horizons Forum and Aerospace Exposition, 2009.

[9] J. Joo, et al., Large-eddy simulation of a compressor rotor, https://api.semanticscholar.org/CorpusID:39311083, 2014.

[10] Dimitrios Papadogiannis, Xavier Garnaud, Unstructured large eddy simulations of the transonic compressor Rotor 37, in: 23rd AIAA Computational Fluid Dynamics Conference, 2017.

[11] Stephan Priebe, et al., Large eddy simulations of a transonic airfoil cascade, in: Turbo Expo: Power for Land, Sea, and Air Volume 10A: Turbomachinery — Axial Flow Fan and Compressor Aerodynamics, June 2022, V10AT29A010.

[12] Stephan Priebe, et al., Large eddy simulation of laminar and turbulent shock/boundary layer interactions in a transonic passage, in: Turbo Expo: Power for Land, Sea, and Air Volume 2A: Turbomachinery, Sept. 2020, V02AT32A005.

[13] Philipp L. Nel, Shock Oscillation Mechanisms of Highly Separated Transitional Shock-Wave/Boundary-Layer Interactions, PhD thesis, TU Berlin, 2025.

[14] Philipp L. Nel, et al., Highly separated transitional shock-wave/boundary-layer interactions: a spatial modal study, Phys. Fluids (ISSN 1070-6631) 36 (11) (Nov. 2024) 116114, https://doi.org/10.1063/5.0239390.

[15] Philipp L. Nel, et al., Shock oscillation mechanism of highly separated transitional shock-wave/boundary-layer interactions, AIAA J. 63 (5) (2025) 1703–1715, https://doi.org/10.2514/1.J064567.

[16] István Z. Reguly, Gihan R. Mudalige, Modernising an industrial CFD application, in: 2020 Eighth International Symposium on Computing and Networking Workshops (CANDARW), 2020, pp. 191–196.

[17] Philipp L. Nel, et al., Towards understanding and resolving natural shock oscillation in transonic compressors, in: Tero Tuovinen, et al. (Eds.), Advanced Computational Methods and Design for Greener Aviation, Springer International Publishing, Cham, ISBN 978-3-031-61109-4, 2024, pp. 75–93.

[18] Tip clearance vortex oscillation, vortex shedding and rotating instabilities in an axial transonic compressor rotor, in: Volume 6: Turbomachinery, Parts A, B, and C. Turbo Expo: Power for Land, Sea, and Air, June 2008, pp. 57–65.

[19] Zhen Li, Yaping Ju, Chuhua Zhang, Quasi-wall-resolved large eddy simulation of transitional flow in a transonic compressor rotor, Aerosp. Sci. Technol. (ISSN 1270-9638) 126 (2022) 107620, https://doi.org/10.1016/j.ast.2022.107620.

[20] Piotr Doerffer, et al., Transition Location Effect on Shock Wave Boundary Layer Interaction: Experimental and Numerical Findings from the TFAST Project, Notes on Numerical Fluid Mechanics and Multidisciplinary Design, vol. 144, Springer, Cham, Switzerland, 2021.

[21] Franck Nicoud, Hideo Toda, Shigeo Kawai, Using the SIGMA model for LES of wall-bounded turbulent flows, J. Comput. Phys. 230 (14) (2011) 5261–5280, https://doi.org/10.1016/j.jcp.2011.03.040.

[22] Nicoud Franck, Frédéric Ducros, Subgrid-scale stress modelling based on the square of the velocity gradient tensor, Flow Turbul. Combust. 62 (3) (1999) 183–200, https://doi.org/10.1023/A:1009995426001.

[23] Joseph Smagorinsky, General circulation experiments with the primitive equations: I. The basic experiment, Mon. Weather Rev. 91 (3) (1963) 99–164, https://doi.org/10.1175/1520-0493(1963)091<0099:GCEWTP>2.3.CO;2.